VU Research Portal

Seismic and Newtonian noise modeling for Advanced Virgo and Einstein Telescope

Bader, M.K.M.

2021

document version
Publisher's PDF, also known as Version of record

Link to publication in VU Research Portal

citation for published version (APA)
Bader, M. K. M. (2021). *Seismic and Newtonian noise modeling for Advanced Virgo and Einstein Telescope*.
[PhD-Thesis - Research and graduation internal, Vrije Universiteit Amsterdam].

Chapter 3

Seismic and Newtonian noise modeling

The performance of terrestrial interferometric gravitational wave detectors at frequencies below 20 Hz is limited by seismic noise. This noise couples to the test masses in two ways, mechanically by moving the mirror suspensions and directly by gravitational attraction. The mechanical coupling of the ground motion can efficiently be suppressed by several orders of magnitude through advanced vibration isolation systems [37]. However, the Newtonian force on the test mass, created by seismically induced mass density fluctuations, cannot be suppressed. This effect on the detector sensitivity is referred to as *Newtonian noise*.

In the following we restrict our consideration to Newtonian noise from the seismic field near the site, assuming that 'trivial' noise generated by local equipment like pumps and air conditioning can be mitigated. Furthermore, we neglect the effect of Newtonian noise from atmospheric pressure variations, which is treated for example in [47]. Estimates of the seismic Newtonian noise for a given detector rely on a model of the geology and on the seismic field near the test masses.

Here we will first introduce seismic wave propagation in both, half-space and horizontal layered geologies, and consider full solutions to the elastodynamic wave equation that are obtained with numerical solver software. The results are used to model an ambient seismic field and to estimate Newtonian noise at a specified detector site, based on measured geology and seismic source distribution.

3.1   Seismic wave propagation

The behavior of soil under dynamic loading conditions is typically complex, anisotropic and non-linear. If the forces that excite a soil profile are small, then it can be assumed that the soil behaves like an elastodynamic medium. This means that the soil obeys Hooke's law and that a force on the medium results in its pure displacement, neglecting irreversible deformation effects. When studying the soil response to ambient noise, a given soil profile can be approximated as a homogeneous half-space or as a horizontally layered medium. In this section we first derive the equations governing wave propagation in homogenous media. If the soil profile is simple, for example in the case of a uniform half-space, then the solutions of the wave equation can be derived analytically. For more complex geologies, standard numerical solving techniques have been derived in seismology. They are discussed in the second part of this section.

3.1.1 The elastodynamic wave equation

Elasticity is the property that enables fluids or solid bodies to resist changes in size and shape when an external force is applied or to return to their original size and shape when the force is removed [105]. The theory of elasticity is a major building block of seismology, as it uses concepts known from classical mechanics such as stress and strain and their connection via Hooke's law to derive the principles of seismic wave propagation through solids such as rocks.

The entity describing the motion of a volume element at location $\vec{x} = (x_1, x_2, x_3)$ inside a medium at time t is a vector field, the so called *displacement field* $\vec{u}(\vec{x}, t)$. If the position of the element changes by an infinitesimal amount with respect to the initial position $\vec{x}_0$, then the displacement field can be Taylor-expanded as [106]

$$\vec{u}(\vec{x}, t) = \vec{u}(\vec{x}_0, t) + \begin{bmatrix} \frac{\partial u_1}{\partial x_1} & \frac{\partial u_1}{\partial x_2} & \frac{\partial u_1}{\partial x_3} \\ \frac{\partial u_2}{\partial x_1} & \frac{\partial u_2}{\partial x_2} & \frac{\partial u_2}{\partial x_3} \\ \frac{\partial u_3}{\partial x_1} & \frac{\partial u_3}{\partial x_2} & \frac{\partial u_3}{\partial x_3} \end{bmatrix} \Bigg|_{\vec{x}_0} \cdot \begin{bmatrix} d_1 \\ d_2 \\ d_3 \end{bmatrix} = \vec{u}(\vec{x}_0, t) + \mathbf{J}\vec{d}, \tag{3.1.1}$$

where $\vec{d} = (d_1, d_2, d_3) = \vec{x} - \vec{x}_0$ is the distance to the initial position. The matrix $\mathbf{J} = \epsilon + \Omega$ can be further expanded into the symmetric *strain tensor* ϵ with components

$$\begin{aligned} \epsilon_{ij} &= \begin{bmatrix} \frac{\partial u_1}{\partial x_1} & \frac{1}{2}\left(\frac{\partial u_1}{\partial x_2} + \frac{\partial u_2}{\partial x_1}\right) & \frac{1}{2}\left(\frac{\partial u_1}{\partial x_3} + \frac{\partial u_3}{\partial x_1}\right) \\ \frac{1}{2}\left(\frac{\partial u_2}{\partial x_1} + \frac{\partial u_1}{\partial x_2}\right) & \frac{\partial u_2}{\partial x_2} & \frac{1}{2}\left(\frac{\partial u_2}{\partial x_3} + \frac{\partial u_3}{\partial x_2}\right) \\ \frac{1}{2}\left(\frac{\partial u_3}{\partial x_1} + \frac{\partial u_1}{\partial x_3}\right) & \frac{1}{2}\left(\frac{\partial u_3}{\partial x_2} + \frac{\partial u_2}{\partial x_3}\right) & \frac{\partial u_3}{\partial x_3} \end{bmatrix} \\ &= \frac{1}{2}\left(\frac{\partial u_j}{\partial x_i} + \frac{\partial u_i}{\partial x_j}\right), \end{aligned} \tag{3.1.2}$$

and the asymmetric *rotation tensor* Ω with components

$$\begin{aligned} \Omega_{ij} &= \begin{bmatrix} 0 & \frac{1}{2}\left(\frac{\partial u_1}{\partial x_2} - \frac{\partial u_2}{\partial x_1}\right) & \frac{1}{2}\left(\frac{\partial u_1}{\partial x_3} - \frac{\partial u_3}{\partial x_1}\right) \\ \frac{1}{2}\left(\frac{\partial u_2}{\partial x_1} - \frac{\partial u_1}{\partial x_2}\right) & 0 & \frac{1}{2}\left(\frac{\partial u_2}{\partial x_3} - \frac{\partial u_3}{\partial x_2}\right) \\ \frac{1}{2}\left(\frac{\partial u_3}{\partial x_1} - \frac{\partial u_1}{\partial x_3}\right) & \frac{1}{2}\left(\frac{\partial u_3}{\partial x_2} - \frac{\partial u_2}{\partial x_3}\right) & 0 \end{bmatrix} \\ &= \frac{1}{2}\left(\frac{\partial u_j}{\partial x_i} - \frac{\partial u_i}{\partial x_j}\right). \end{aligned} \tag{3.1.3}$$
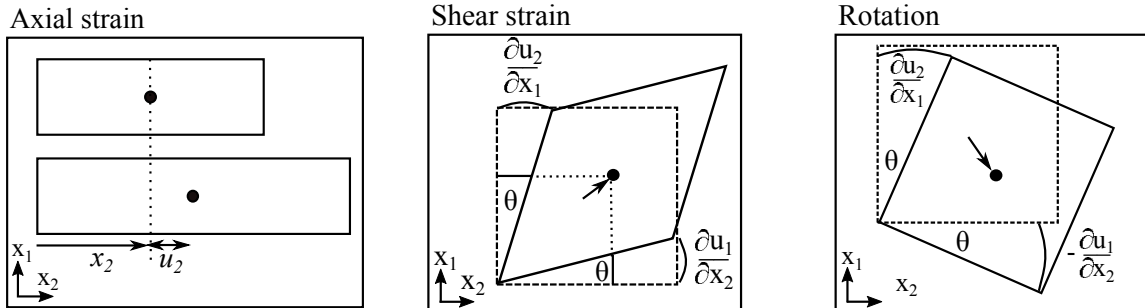
Figure 3.1: *Left: The axial strain is the deformation of an object parallel to the axis of the displacement, $\frac{\partial u_2}{\partial x_2}$ for this example. Middle: The shear strain as the rate of change in an object's angles in a two-dimensional plane. Right: If both derivatives $\frac{\partial u_1}{\partial x_2}$ and $\frac{\partial u_2}{\partial x_1}$ have an opposite sign, the shape of the volume element does not change and a pure rotation occurs.*

Strain describes how positions of points in a continuum are changed through a displacement field $\vec{u}(\vec{x}, t)$. The diagonal elements of the tensor are called the *axial strain* and they describe the ratio of change in deformation parallel to the direction of displacement with respect to the original form of the object (Fig. 3.1, left panel). The off-diagonal elements of the strain tensor are called the *shear strain* and they are the ratio in change of deformation in the direction perpendicular to the axis of the displacement acting on the object. For a more intuitive understanding consider the two-dimensional case with $x_3 = 0$, where the axial strain is zero ($\frac{\partial u_i}{\partial x_i} = 0$) and where both derivatives $\frac{\partial u_1}{\partial x_2}$ and $\frac{\partial u_2}{\partial x_1}$ are equal (Fig. 3.1, central panel). Since we are considering infinitesimal small displacements, the deformation angles can be expressed as

$$\theta \approx \tan(\theta) = \frac{\partial u_1}{\partial x_2} = \frac{\partial u_2}{\partial x_1}. \tag{3.1.4}$$

The sum of both deformation angles are then the elements of the shear tensor and its elements therefore represent the deformed object's angles with respect to the initial angles. In contrast the elements of the rotation tensor $\mathbf{\Omega}$ cause a pure rotation, which is represented by the opposite signs of the derivatives (Fig. 3.1, right panel) and in Eq. (3.1.3).

The force per unit area, acting on an infinitesimal small plane that is characterized by the normal vector $\hat{n}$, is called the *traction* $\vec{t}$ (Fig. 3.2). This definition, which is common in seismology, means that a compressional force is negative and an extensional force is positive [106]. A force on a plane of the medium leads to internal forces, which are called *stress*. The ith component of the traction, t_i, across the plane with normal vector $\hat{n}$, with components n_j, is then represented by the element σ_{ij} of the *stress tensor* $\mathbf{\sigma}$, so that the expression $t_i = \sigma_{ij} n_j$ holds.
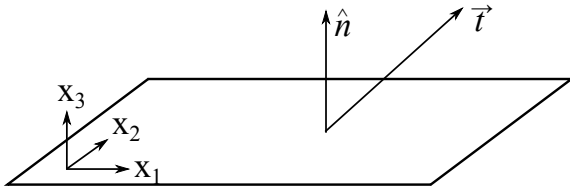

Figure 3.2: *The traction $\vec{t}$ is a force per unit area on the surface with normal vector $\hat{n}$, where an extensional force is positive, while a compressional force is negative.*

External forces on the medium lead to displacement and deformation and hence stress and strain are inevitably linked to each other. Hooke's law states that stress and strain are proportional as

$$\sigma_{ij} = \sum_{kl} C_{ijkl} \epsilon_{kl}, \tag{3.1.5}$$

where the proportionality C_{ijkl} is given by the *elasticity tensor*. For an isotropic medium the elasticity tensor can be expressed in terms of the so called Lamé parameters μ and λ, which are defined as

$$\mu \equiv \frac{E}{2(1+\nu)}, \quad \lambda \equiv \frac{E\nu}{(1+\nu)(1-2\nu)}, \tag{3.1.6}$$

where E represents the Young's modulus and ν the Poisson ratio. As the Lamé parameters relate to material properties, they can be used to describe the elastic restoring force of a medium as

$$C_{ijkl} = \lambda \delta_{ij}\delta_{kl} + \mu(\delta_{ik}\delta_{jl} + \delta_{ik}\delta_{jl}), \tag{3.1.7}$$

where δ_{ij} denotes the Kronecker delta. This allows to re-express Eq. (3.1.5) as

$$\sigma_{ij} = \sum_{k} \lambda \epsilon_{kk} \delta_{ij} + 2\mu \epsilon_{ij}. \tag{3.1.8}$$

The total force $\partial\vec{F}$ per infinitesimal volume element $\partial V = \partial x_1 \partial x_2 \partial x_3$ can then be derived by multiplying the individual traction vectors $\vec{t}_j$ with the surface area they are acting on as

$$\frac{\partial\vec{F}}{\partial V} = \frac{\partial\vec{t}_1 \cdot \partial A_{23}}{\partial x_1 \partial x_2 \partial x_3} + \frac{\partial\vec{t}_2 \cdot \partial A_{13}}{\partial x_1 \partial x_2 \partial x_3} + \frac{\partial\vec{t}_3 \cdot \partial A_{12}}{\partial x_1 \partial x_2 \partial x_3} = \sum_{j=1}^{3} \frac{\partial\vec{t}_j}{\partial x_j}, \qquad (3.1.9)$$

where $\partial A_{kl} = \partial x_k \partial x_l$, with $j \neq k \neq l$, represents the infinitesimal surface that the traction $\vec{t}_j$ is defined across. Using this in Eq. (3.1.9) allows to formulate the ith component of the force density $\frac{\partial F_i}{\partial V} = \rho \cdot \frac{\partial^2 u_i}{\partial t^2}$ as

$$\frac{\partial F_i}{\partial V} = \sum_{j=1}^{3} \frac{d\sigma_{ij}}{dx_j} = \rho\frac{\partial^2 u_i}{\partial t^2}, \qquad (3.1.10)$$

where $\rho = \frac{\partial m}{\partial V}$ represents the density of the medium. In addition to external forces, internal forces called body forces can act on the volume element. Body forces encompass for example gravity and electromagnetic fields. They are typically small in comparison to those in seismic wave fields and are therefore neglected in this treatment.

Making use of Eq. (3.1.8) and the relation between strain and displacement (Eq. (3.1.2)) allows to reformulate Eq. (3.1.10) for the ith vectorial component in terms of the displacement field as

$$\sum_{j=1}^{3} \left((\lambda + \mu)\frac{\partial^2 u_j}{\partial x_i \partial x_j} + \mu\frac{\partial^2 u_i}{\partial x_j \partial x_j} \right) = \rho\frac{\partial^2 u_i}{\partial t^2}, \qquad (3.1.11)$$

which is called the *elastodynamic wave equation*. The vectorial expression of the elastodynamic wave equation is written as

$$(\lambda + \mu)\nabla(\nabla \cdot \vec{u}) + \mu\nabla^2\vec{u} = \rho\frac{\partial^2\vec{u}}{\partial t^2}, \qquad (3.1.12)$$

where $\nabla = (\frac{\partial}{\partial x_1}, \frac{\partial}{\partial x_2}, \frac{\partial}{\partial x_3})$ represents the Nabla operator and where $\nabla\vec{u}$, $\nabla \cdot \vec{u}$ and $\nabla \times \vec{u}$ denote the gradient, the divergence and the curl of the vector field $\vec{u}$.

3.1.2 Analytical solutions of the elastodynamic wave equation

Solutions of the elastodynamic wave equation depend on the composition of the medium and on the imposed boundary conditions. Analytical solutions only exist in very special cases, for example for two-dimensional, uniform problems. For all other types of problems, for example for the solution in multilayered three-dimensional media, special analysis techniques and numerical solutions and methods need to be employed to solve the wave equation. Nevertheless, it is instructive to study the analytical solutions as they give an overview of the fundamental wave types that exist. The analytical solutions of the wave equation are extensively treated in standard literature for seismology [106–108] and in the following a short derivation of the different solutions based on this literature will be given.

Two types of boundary conditions are used in seismology [107]: *kinematic boundary conditions* refer to the study of motion and therefore restrict the displacement field. For a boundary between two solid materials it is required that the displacement field is continuous for all three components throughout the boundary. Discontinuity for example in the horizontal components

means that slip is possible between the two materials, which is not the case for the solid rock geologies that are considered in this work. *Dynamic boundary conditions* refer to the study of forces on a system and therefore require continuity of the traction vector. As the vector normal to the surface of a medium is by definition pointing outward of the medium, this means that the stresses across an interface are equal in magnitude, but opposite in sign, which is only true if the horizontal stress components across the surface are continuous.

Body waves

At first an unbound, homogeneous medium is considered. Since the differential equation given by Eq. (3.1.11) is not trivial to solve, solutions are typically obtained as a sum of solutions of simpler equations. One method, which is common practice in seismology, is to decompose the displacement vector field $\vec{u}$ via the *Helmholtz decomposition* [109] in terms of the scalar potential Φ and the vector potential $\vec{\Psi} = (\Psi_1, \Psi_2, \Psi_3)$ as

$$\vec{u} = \nabla\Phi + \nabla \times \vec{\Psi} = \begin{bmatrix} \frac{\partial \Phi}{\partial x_1} + \frac{\partial \Psi_3}{\partial x_2} - \frac{\partial \Psi_2}{\partial x_3} \\ \frac{\partial \Phi}{\partial x_2} + \frac{\partial \Psi_1}{\partial x_3} - \frac{\partial \Psi_3}{\partial x_1} \\ \frac{\partial \Phi}{\partial x_3} + \frac{\partial \Psi_2}{\partial x_1} - \frac{\partial \Psi_1}{\partial x_2} \end{bmatrix}, \qquad (3.1.13)$$

where $\nabla\Phi$ represents a curl-free field and $\nabla \times \vec{\Psi}$ a divergence-free vector field and where the curl has been calculated in a right-handed coordinate system. This decomposition allows to rewrite the elastodynamic wave equation in terms of two uncoupled equations as

$$\nabla^2 \Phi = \frac{1}{v_P^2} \frac{\partial^2}{\partial t^2} \Phi \rightarrow v_P = \sqrt{\frac{\lambda + 2\mu}{\rho}}, \qquad (3.1.14)$$

$$\nabla^2 \vec{\Psi} = \frac{1}{v_S^2} \frac{\partial^2}{\partial t^2} \vec{\Psi} \rightarrow v_S = \sqrt{\frac{\mu}{\rho}}, \qquad (3.1.15)$$

where v_P and v_S are the velocities of the fundamental waves, which are solutions to the corresponding equations. For simplicity plane wave solutions in Cartesian coordinates are assumed. In Cartesian coordinates, plane waves are especially simple since all coordinate contributions which are perpendicular to the direction of propagation are constants. Two types of waves are solutions to the above set of equations (Fig. 3.3, left panel). First, consider a wave propagating in x_1-direction, where the particle displacement is parallel to the direction of motion. This type of wave is called a *pressure* (P)-wave and the displacement field is of the form

$$\vec{u}_P(\vec{x}, t) = \left(f(t - \frac{x_1}{v_P}), 0, 0\right) = \left(\frac{\partial \Phi}{\partial x_1}, 0, 0\right), \qquad (3.1.16)$$

where f is some function describing the amplitude of the displacement. This is a solution of Eq. (3.1.14), which is called the wave equation for P-waves and $\nabla\Phi$ is the P-wave contribution of the displacement field. A plane wave propagating in the x_1-direction with particle motion perpendicular to the direction of motion is called a *shear* (S)-wave and it can be defined in two ways

$$\vec{u}_{SV}(\vec{x}, t) = \left(0, f(t - \frac{x_1}{v_S}), 0\right) = \left(0, -\frac{\partial \Psi_3}{\partial x_1}, 0\right),$$

$$\vec{u}_{SH}(\vec{x}, t) = \left(0, 0, f(t - \frac{x_1}{v_S})\right) = \left(0, 0, \frac{\partial \Psi_2}{\partial x_1}\right), \qquad (3.1.17)$$

where all derivatives other than in the direction of propagation are zero. Both equations are independent solutions to Eq. (3.1.15), and they are referred to as the two polarizations of the S-wave. Their polarization is determined by the plane that is spanned by the particle motion and propagation direction. If it is parallel to a surface or interface in the medium it is called the horizontally polarized shear (SH) wave and if the plane is perpendicular to an interface or surface the wave is called a vertically polarized shear (SV) wave. The term $\nabla \times \vec{\Psi}$ in the displacement field is referred to as the S-wave contribution to the displacement field.
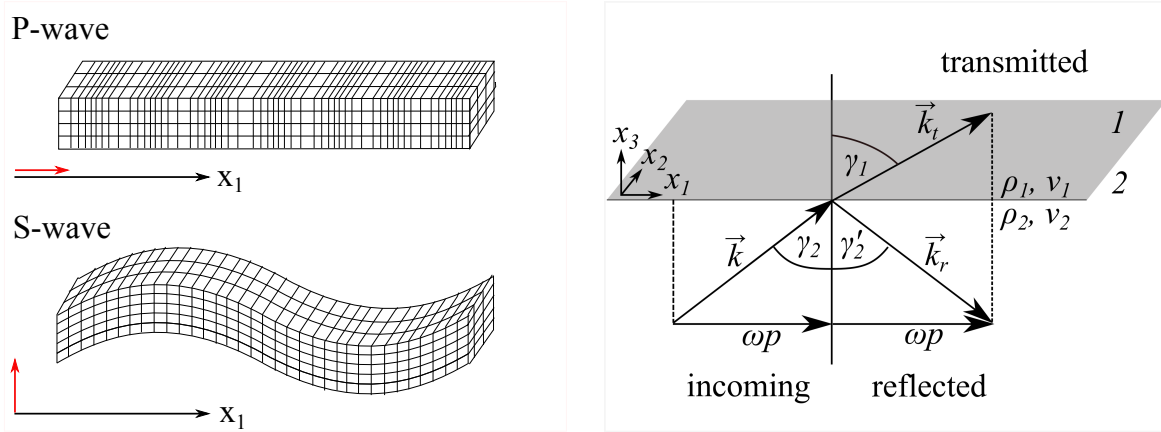

Figure 3.3: *Left: Plane P- and S-wave propagation in an unbounded medium. The direction of propagation is along x_1 and the direction of particle displacement is indicated with a red arrow. Right: Visualization of Snell's law for seismic waves at an interface with two media of density ρ_1 and ρ_2, and velocities v_1 and v_2. The wave vectors of the incoming, reflected and transmitted wave are denoted by $\vec{k}$, $\vec{k}_r$ and $\vec{k}_t$. The horizontal component of the wave vector is ωp, where p is called the slowness.*

Interactions at material boundaries

A realistic soil model consists of layers with different material properties. If body waves encounter an interface between two different materials, then transmission, reflection and mode conversion can occur. To study these phenomena, consider in medium 2 an incoming plane wave, where the wave vector $\vec{k}$ is confined to the x_1x_3-plane (Fig. 3.3, right panel). For such a wave the displacement field is given by

$$\vec{u}(\vec{x},t) = \vec{u}_0(\vec{x}) \cdot e^{i(\omega t - \vec{k}\cdot\vec{x})} = \vec{u}_0(\vec{x}) \cdot e^{i\omega\left(t - \frac{1}{v_2}(x_1\sin\gamma_2 + x_3\cos\gamma_2)\right)}, \qquad (3.1.18)$$

where the wave vector is $\vec{k} = \frac{2\pi f}{v_2}(\sin\gamma_2, 0, \cos\gamma_2)$ with wave oscillation frequency f, wave speed v_2 in the direction of propagation at the location $\vec{x} = (x_1, x_2, x_3)$ and where $|\vec{k}| = \frac{\omega}{v_2}$ holds for the wave vector. The reflected and transmitted displacements are, respectively,

$$\vec{u}_r(\vec{x},t) = \vec{u}_{r,0}(\vec{x}) \cdot e^{i\omega\left(t - \frac{1}{v_2}(x_1\sin\gamma_2' - x_3\cos\gamma_2')\right)},$$

$$\vec{u}_t(\vec{x},t) = \vec{u}_{t,0}(\vec{x}) \cdot e^{i\omega\left(t - \frac{1}{v_1}(x_1\sin\gamma_1 + x_3\cos\gamma_1)\right)}. \qquad (3.1.19)$$

The kinematic boundary condition requires the horizontal (in this example the x_1-) component of the incoming, reflected and transmitted wave vector to be continuous and as a result Snell's

law for seismic wave propagation in solid media is obtained as

$$p = \frac{\sin \gamma_2}{v_2} = \frac{\sin \gamma_2'}{v_2} = \frac{\sin \gamma_1}{v_1}, \tag{3.1.20}$$

where the inverse surface velocity p, or horizontal *slowness*, is conserved across the interface. Equation (3.1.20) only holds when $\gamma_2 = \gamma_2'$.

Since the wave propagates in the $x_1 x_3$-plane, the displacement field is constant in x_2. This means that derivatives of the potentials with respect to x_2 are zero. The amplitude $\vec{u}_0$ of the incoming field can then be formulated based on Eq. (3.1.13) in terms of the potentials as

$$(u_{0,1}, u_{0,2}, u_{0,3}) = \left(\frac{\partial \Phi}{\partial x_1} - \frac{\partial \Psi_2}{\partial x_3}, \quad \frac{\partial \Psi_1}{\partial x_3} - \frac{\partial \Psi_3}{\partial x_1}, \quad \frac{\partial \Phi}{\partial x_3} + \frac{\partial \Psi_2}{\partial x_1} \right). \tag{3.1.21}$$

It can be seen that the displacements in the $x_1 x_3$-plane are coupled via the wave potentials and that they are completely independent from the displacement $u_{0,2}$. Hence two independent systems can be defined: the system with the horizontally polarized S-wave (SH-system) and the system with a superposition of P-wave and vertically polarized S-wave (P/SV-system).
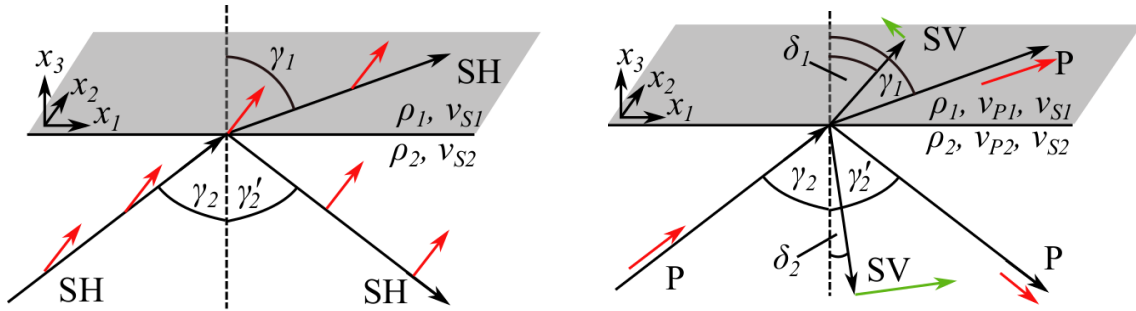

Figure 3.4: *Left: Reflection of an SH-wave on an interface between two layers. The displacement direction (red, parallel to the x_2-axis) is perpendicular to the direction of propagation and does not change direction when interacting with the interface. Right: The displacement of an incoming P-wave changes direction when the P-wave interacts with an interface (red). The direction of displacement on the interface is then only conserved, if an additional SV-wave (green) is generated. This coupling between P- and SV-waves is known as mode conversion.*

If an SH-wave encounters an interface it is reflected and transmitted. The direction of the displacement field remains unchanged even though the propagation direction of the wave may change. The displacement stays unaffected, because it is confined to the plane perpendicular to the direction of propagation (Fig. 3.4, left). Considering the boundary conditions, the amplitude reflection and transmission coefficients of the SH-wave, r_{SH} and t_{SH} respectively, can be derived as [107]

$$r_{SH} = \frac{\rho_1 v_{S1} \cos \gamma_1 - \rho_2 v_{S2} \cos \gamma_2}{\rho_2 v_{S2} \cos \gamma_2 + \rho_1 v_{S1} \cos \gamma_1}, \quad t_{SH} = \frac{2\rho_2 v_{S2} \cos \gamma_2}{\rho_2 v_{S2} \cos \gamma_2 + \rho_1 v_{S1} \cos \gamma_1}. \tag{3.1.22}$$

In the P/SV-system, P- and SV-waves are coupled and conversions between both modes occur when the waves interact with an interface (Fig. 3.4, right panel). Consider an incoming P-wave that interacts with an interface. The displacement of a P-wave is parallel to the direction of propagation, so as the direction of propagation changes for the transmitted (reflected) P-wave, the direction of displacement also changes. The conservation of displacement at the interface

gives rise to a wave with displacement in the SV-direction. Reflection and transmission coefficients for all waves have been derived in [107] (p.139ff). For completeness the P- and SV-wave amplitude reflection coefficients at a free surface for an incoming P-wave will be given here as

$$r_{SV} = \frac{4v_{S2}^2 p \frac{\cos \gamma_2}{v_{P2}}(1 - 2v_{S2}^2 p^2)}{4v_{S2}^4 p^2 \frac{\cos \gamma_2}{v_{P2}} \frac{\cos \delta_2}{v_{S2}} + (1 - 2v_{S2}^2 p^2)^2}, \quad r_P = \frac{4v_{S2}^4 p^2 \frac{\cos \gamma_2}{v_{P2}} \frac{\cos \delta_2}{v_{S2}} - (1 - 2v_{S2}^2 p^2)^2}{4v_{S2}^4 p^2 \frac{\cos \gamma_2}{v_{P2}} \frac{\cos \delta_2}{v_{S2}} + (1 - 2v_{S2}^2 p^2)^2}. \quad (3.1.23)$$

Surface waves

Surface waves attenuate fast with increasing depth and propagate parallel to the surface. The mathematical description of such a singular wave traveling in the x_1-direction is of the form

$$\vec{u}(\vec{x}, t) = f(x_3)e^{i\omega(t - \frac{x_1}{v})}, \quad (3.1.24)$$

where v represents the velocity in the direction of propagation. Surface waves are a superposition of body waves at the free surface and under certain boundary conditions, both the SH and the P/SV-system can generate surface waves. The surface waves of the P/SV-system have been studied by J. Rayleigh [110], hence they are called *Rayleigh waves*. He has shown that in a homogeneous half-space, surface waves can exist by interfering P- and SV-waves if the velocities fulfil

$$\left(\frac{v_R^2}{v_S^2}\right)^3 - 8\left(\frac{v_R^2}{v_S^2}\right)^2 + 8\left(\frac{2 - \nu}{1 - \nu}\right)\left(\frac{v_R^2}{v_S^2}\right) - \frac{8}{1 - \nu} = 0 \quad (3.1.25)$$

and obey the condition that $v_R < v_S < v_P$. With this condition the respective horizontal and vertical particle displacements of the Rayleigh wave are obtained as

$$u_1(\vec{x}, t) = ik_R A \left(e^{qk_R x_3} - \frac{2pq}{1 + p^2}e^{pk_R x_3}\right)e^{i(\vec{k_R} \cdot \vec{x} - \omega t)},$$

$$u_3(\vec{x}, t) = -qk_R A \left(e^{qk_R x_3} - \frac{2}{1 + p^2}e^{pk_R x_3}\right)e^{i(\vec{k_R} \cdot \vec{x} - \omega t)}, \quad (3.1.26)$$

where $k_R = |\vec{k_R}|$ represents the wave vector of the Rayleigh wave, A an arbitrary wave amplitude, and the velocity ratios are defined as

$$q \equiv \sqrt{1 - \frac{v_R^2}{v_P^2}}, \quad p \equiv \sqrt{1 - \frac{v_R^2}{v_S^2}}. \quad (3.1.27)$$

The particle motion of a Rayleigh wave is elliptical and counter-clockwise at the surface (Fig. 3.5, left panel). At a depth of about $0.2\ \lambda_R$ the sign of the phase between horizontal and vertical motion changes, leading to a change of the particle rotation to the clock-wise direction. The horizontal amplitude of the Rayleigh wave attenuates strongly with depth (Fig. 3.5, right panel). At $0.2\ \lambda_R$ a zero-crossing is reached, which corresponds to the shift in phase. Vertical amplitudes experience a short amplitude increase close below the surface before they attenuate. At the depth of one Rayleigh wavelength, both amplitudes are attenuated to less than 20% of their surface value.

Rayleigh waves also exist if the medium is not a homogeneous half-space, but is composed of layers with different material properties [108]. In this case a similar, but frequency dependent condition for the velocities similar to Eq. (3.1.25) can be formulated. This so called *dispersion curve* depends on the number, thickness and material properties of the subsurface layers. A
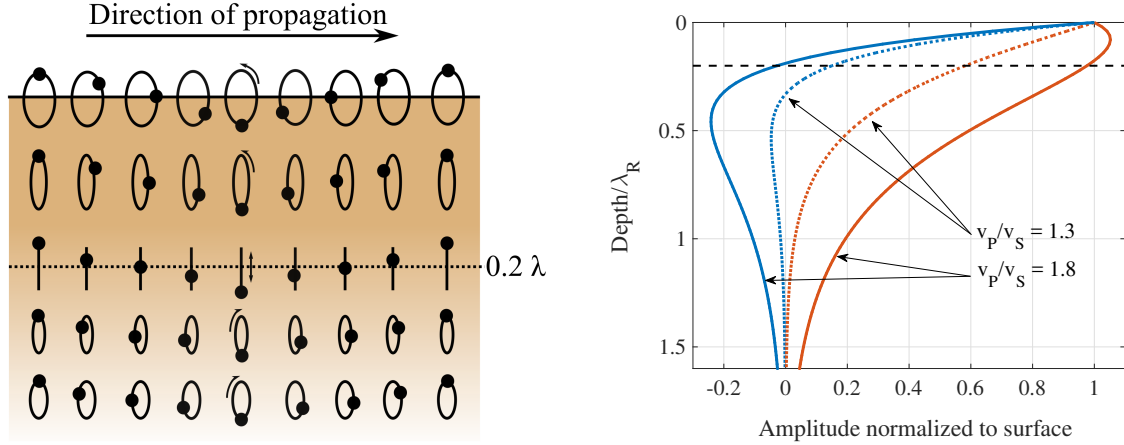
Figure 3.5: *Left: Particle motion of a Rayleigh wave propagating from left to right. One horizontal wavelength λ is shown, and the dots represent all particle locations at the same fixed point in time. On the surface the particle motion is counter-clockwise, changing to a purely vertical motion at about $0.2 \lambda_R$ and becoming a clockwise rotation at greater depths. The time behavior at a fixed location is given by looking from right to left. Figure adapted from [106]. Right: Attenuation of horizontal (blue) and vertical (red) Rayleigh wave amplitudes with depth. The horizontal motion attenuates faster than the vertical motion and changes sign close to a depth of $0.2 \lambda_R$ (black dashed line). Vertical particle motion slightly increases before being strongly attenuated with increasing depth. The peak amplitude depends on the ratio of P- and S-wave speeds in the medium. Both types of motion are suppressed to about 20% of their surface value at a depth of one Rayleigh wavelength.*

general, analytical formulation of the dispersion curve is not possible. It is characteristic for a soil profile, a property which is exploited in seismology and exploration geology to image subsurface composition from surface measurements.

Under certain conditions, the SH-system can produce surface waves, called *Love* waves, as well. It can be shown that in a half-space the boundary condition of zero stress on the surface can only be fulfilled if the amplitude of the wave is zero [106]. This means that Love waves cannot exist in a homogeneous half-space geology, but they can exist in a layered medium. It can be shown [106] that in a medium that consists of one layer of thickness d (medium 1) on a half-space (medium 2) the condition for the Love wave speed v_L is

$$\tan\left(\frac{d \cdot \omega}{v_L}\sqrt{\frac{v_L^2}{v_{S1}^2} - 1}\right) = \frac{\rho_2 v_{S2}^2 \sqrt{1 - \frac{v_L^2}{v_{S2}^2}}}{\rho_1 v_{S1}^2 \sqrt{1 - \frac{v_L^2}{v_{S1}^2}}}, \tag{3.1.28}$$

where ρ_i represents the density, v_{Si} the S-wave speed in the layer ($i = 1$) or half-space ($i = 2$), and ω the angular frequency of the wave. To obtain the Love wave dispersion curve, this equation needs to be solved for $v_L = v_L(\omega)$. The tangent is a harmonic function ($\tan(x) = \tan(x+n\pi)$) and therefore the solution of Eq. (3.1.28) is not unique. The solutions of Eq. (3.1.28) are referred to as the modes of the wave, where the solution for $n = 0$ is called the *fundamental mode*, and all other solutions with $n > 0$ are called *higher order modes*. Fundamental and higher order modes exist and have been measured for Love and for Rayleigh waves [111, 112]. The physical interpretation of higher order modes beyond the mathematical understanding is still de-
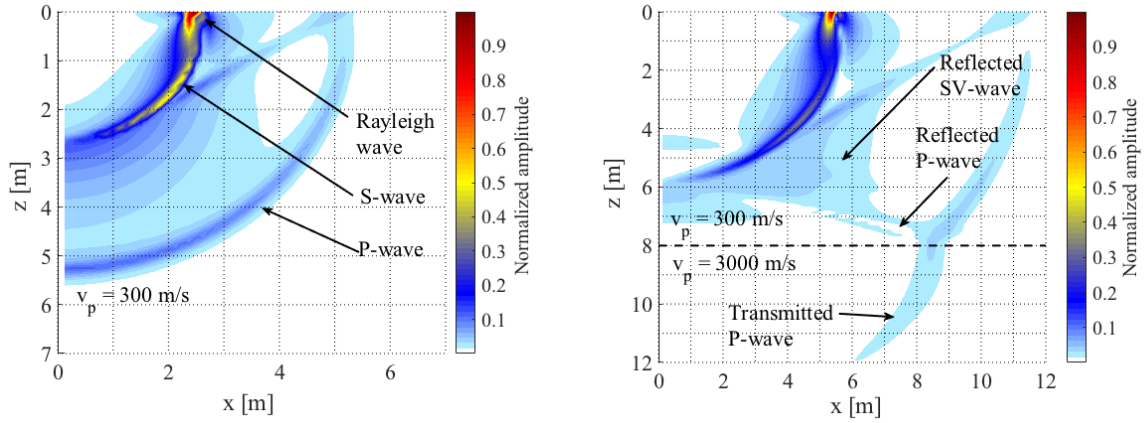
Figure 3.6: *Left: P- and S-waves generated by a point source in a homogeneous half-space spread over the entire volume while the energy of Rayleigh waves is constrained to a circle in the surface plane. Right: The layer interface leads to additional effects like wave reflection, transmission and mode conversion.*

bated within the geophysics community. Most commonly they are interpreted as a phenomenon of constructive interference of waves that are reflected multiple times within the layers of a heterogeneous material [107, 113]. The amplitude and energy distribution of higher order modes depends on many site-specific factors such as geology, layer material properties, source mechanism, type and distance. Typically the fundamental mode is more dominant in geologies where the S-wave velocity increases gradually with depth, while geologies with high velocity contrasts in layers at shallow depths can lead to an increased amplitude of the higher order modes.

Attenuation and energy spreading

Attenuation of seismic waves is connected to the concept of energy loss during propagation. Energy of a seismic wave can be dissipated by geometric or by material damping. *Geometric damping* is a result of energy spreading over an increasing area of the wavefront. In reality, seismic waves are rarely plane waves, but they are emitted by sources and spread equally in all three spatial dimensions (Fig. 3.6). Hence, body waves are spherical waves. With increasing distance r from the excitation point their energy decreases with $1/r^2$ and their amplitude with $1/r$. Surface waves propagate along the two surface dimensions, hence their energy is reduced by $1/r$ and their amplitude by $1/\sqrt{r}$. *Material damping* contributes to energy loss due to inelastic processes and internal friction within the medium during wave propagation. This can for example be attributed to internal heating or to deformation of the material. Material damping of P- and S-waves is described by the wave-dependent quality factors Q_P and Q_S [106]. The quality factor is inversely related to the attenuation: regions with high quality factor exhibit low amplitude attenuation and regions with small quality factor exhibit high amplitude attenuation. For a wave propagating in the $\vec{x}$-direction the amplitude attenuation by material damping is given by

$$u_c(x) = e^{-\frac{\vec{k} \cdot \vec{x}}{2 Q_c}}, \qquad (3.1.29)$$

where the subscript $c \in (P, S)$ either represents the P- or the S-wave material quality factor, respectively. With Eq (3.1.18) the total wave amplitude of a plane wave with material damping

can then be expressed as

$$\vec{u}(\vec{x}, t) = \vec{u}_0(\vec{x}) \cdot u_c(x) \cdot e^{i(\omega t - \vec{k} \cdot \vec{x})}.$$ (3.1.30)

3.1.3 The stiffness matrix method for horizontally stratified soil profiles

Analytical solutions of the wave equation for a multilayered medium with arbitrary boundary conditions do not exist. Hence, one needs to rely on finite element analysis or other numerical tools to derive the displacement field and associated stress components of complex soil profiles. Standard methods to solve these type of problems are the *propagator matrix* method by Haskell and Thomson [114, 115] and the closely related *direct stiffness* method [116]. The direct stiffness method has several advantages, for instance it involves half the number of degrees of freedom compared to the propagator matrix method. This means that it is computationally twice as fast as the propagator matrix method, hence it is typically integrated in numerical solver software like the Matlab Elastodynamics toolbox (EDT) [117]. Furthermore, the direct stiffness method naturally allows to derive the normal modes of the soil profile from the wave equation and the computation of the dynamic soil response to source excitations, which make it ideal for the purpose of seismic field modeling. The direct stiffness method is based on a transformation of the wave equation from the space-time domain to the wave number-frequency domain, where for each layer a stiffness matrix can be formulated [118, 119]. Superposition of the stiffness matrices from each layer allows the exact mathematical reformulation of the full wave equation as an eigenvalue problem. The numerical solution of the eigenvalue problem and the inverse transformation to the space-time domain gives the displacement field vector and stress components at any specified receiver coordinate.

For a conceptual understanding of the steps in the numerical solving analysis we consider the case of plane wave propagation in a horizontally stratified medium, with the wave vector lying in the $x_1 x_3$-plane, where x_1 indicates the horizontal and x_3 the vertical direction in Cartesian coordinates. This approach is expanded to the three-dimensional representation in spherical coordinates for example in [118, 119]. In this example the displacement in the x_2-direction is constant and all derivatives in Eq. (3.1.12) with respect to $\partial/\partial x_2$ are zero. For simplicity the x_2-component will therefore be dropped in the following.

The Fourier transform allows to transform between the time-domain representation of a function $f(x_1, t)$ and the frequency-domain representation $\hat{f}(x_1, \omega)$ of the function as

$$\hat{f}(x_1, \omega) = \mathcal{F}(f(x_1, t), \omega) = \int_{-\infty}^{\infty} e^{-i\omega t} f(x_1, t) dt$$ (3.1.31)

$$f(x_1, t) = \mathcal{F}^{-1}(\hat{f}(x_1, \omega), t) = \frac{1}{2\pi} \int_{-\infty}^{\infty} e^{i\omega t} \hat{f}(x_1, \omega) d\omega,$$ (3.1.32)

where $\mathcal{F}$ is the forward and $\mathcal{F}^{-1}$ is the inverse transformation [118]. A transformation between the horizontal space and the horizontal wave number domain is further defined as

$$\tilde{f}(k_{x_1}, t) = \mathcal{F}(f(x_1, t), k_{x_1}) = \int_{-\infty}^{\infty} e^{-i k_{x_1} x_1} f(x_1, t) dx_1$$ (3.1.33)

$$f(x_1, t) = \mathcal{F}^{-1}(\hat{f}(k_{x_1}, t), x_1) = \frac{1}{2\pi} \int_{-\infty}^{\infty} e^{i k_{x_1} x_1} \tilde{f}(k_{x_1}, t) dk_{x_1},$$ (3.1.34)

where k_{x_1} is the horizontal wave number. In case of three-dimensional wave propagation in spherical symmetrical geometries, Hankel transformations are used [118]. For a wave propagating in the x_1x_3-plane, the horizontal wave number k_{x_1} of P- and S-waves are then defined as

$$\vec{k}_P = (k_{x_1}, k_{P,x_3}) \rightarrow |\vec{k_P}| = \frac{\omega}{v_P} = \sqrt{k_{x_1}^2 + k_{P,x_3}^2}, \tag{3.1.35}$$

$$\vec{k}_S = (k_{x_1}, k_{S,x_3}) \rightarrow |\vec{k_S}| = \frac{\omega}{v_S} = \sqrt{k_{x_1}^2 + k_{S,x_3}^2}. \tag{3.1.36}$$

Displacement and stress in a homogeneous medium

The elastodynamic wave equation for a plane wave in the x_1x_3-plane in a homogeneous medium can then be derived from Eq. (3.1.12) in the frequency-wave number domain following [118] as

$$-k_{x_1}^2 \mathbf{A}\vec{\mathfrak{u}} - k_{x_1}\mathbf{B}\frac{\partial \vec{\mathfrak{u}}}{\partial x_3} + \mathbf{C}\frac{\partial^2 \vec{\mathfrak{u}}}{\partial x_3^2} = -\omega^2 \rho \vec{\mathfrak{u}}, \text{ where} \tag{3.1.37}$$

$$\mathbf{A} = \begin{bmatrix} \lambda + 2\mu & 0 & 0 \\ 0 & \mu & 0 \\ 0 & 0 & \mu \end{bmatrix}, \mathbf{B} = \begin{bmatrix} 0 & 0 & -(\lambda+\mu) \\ 0 & 0 & 0 \\ \lambda+\mu & 0 & 0 \end{bmatrix}, \mathbf{C} = \begin{bmatrix} \mu & 0 & 0 \\ 0 & \mu & 0 \\ 0 & 0 & \lambda+2\mu \end{bmatrix},$$

where $\vec{\mathfrak{u}} = (u_1(k_{x_1}, x_3, \omega), u_2(k_{x_1}, x_3, \omega), -iu_3(k_{x_1}, x_3, \omega))$ represents the modified displacement vector in the frequency-wave number domain representation (for the derivation see Appendix A). The x_3-component of the displacement vector has been rewritten as $u_3 \rightarrow -iu_3$, to allow for a symmetric formulation of the stiffness matrix later. For readability, all parameter dependencies have been dropped. It can be shown [118] that the solution to Eq. (3.1.37) is of the form

$$\vec{\mathfrak{u}} = \begin{bmatrix} \mathbf{R}_u \mathbf{E}^{-1} & \mathbf{R}_d \mathbf{E} \end{bmatrix} \begin{bmatrix} \vec{\mathfrak{a}}_u \\ \vec{\mathfrak{a}}_d \end{bmatrix}, \text{ where} \tag{3.1.38}$$

$$\mathbf{R}_u = \begin{bmatrix} 1 & 0 & -p \\ 0 & 1 & 0 \\ -q & 0 & 1 \end{bmatrix}, \mathbf{R}_d = \begin{bmatrix} 1 & 0 & p \\ 0 & 1 & 0 \\ q & 0 & 1 \end{bmatrix}, \mathbf{E} = \begin{bmatrix} e^{k_{x_1}qx_3} & 0 & 0 \\ 0 & e^{k_{x_1}px_3} & 0 \\ 0 & 0 & e^{k_{x_1}px_3} \end{bmatrix},$$

where the $\vec{\mathfrak{a}} = (\mathfrak{a}_P, \mathfrak{a}_{SH}, \mathfrak{a}_{SV})$ are the complex wave potential amplitudes of the P-, SH- and SV waves respectively, with the subscript d indicating a wave propagating downward in the negative x_3-direction and the subscript u indicating a wave propagating upward in the positive x_3-direction and where p and q are as defined in Eq. (3.1.27). The modified stress components $\vec{\mathfrak{s}} = (\sigma_{13}, \sigma_{23}, -i\sigma_{33})$ on a horizontal layer that are associated with this displacement are derived from the relationships between displacement, strain and stress, Eq. (3.1.2) and Eq. (3.1.5) respectively. Transforming these equations to the frequency-wave number domain and using Eq. (3.1.38) gives

$$\vec{\mathfrak{s}} = k_{x_1}\mu[-\mathbf{Q}_u\mathbf{E}^{-1} \quad \mathbf{Q}_d\mathbf{E}] \begin{bmatrix} \vec{\mathfrak{a}}_u \\ \vec{\mathfrak{a}}_d \end{bmatrix}, \text{ where} \tag{3.1.39}$$

$$\mathbf{Q}_u = \begin{bmatrix} 2q & 0 & -(1+p^2) \\ 0 & p & 0 \\ -(1+p^2) & 0 & 2p \end{bmatrix}, \mathbf{Q}_d = \begin{bmatrix} 2q & 0 & 1+p^2 \\ 0 & p & 0 \\ 1+p^2 & 0 & 2p \end{bmatrix}.$$
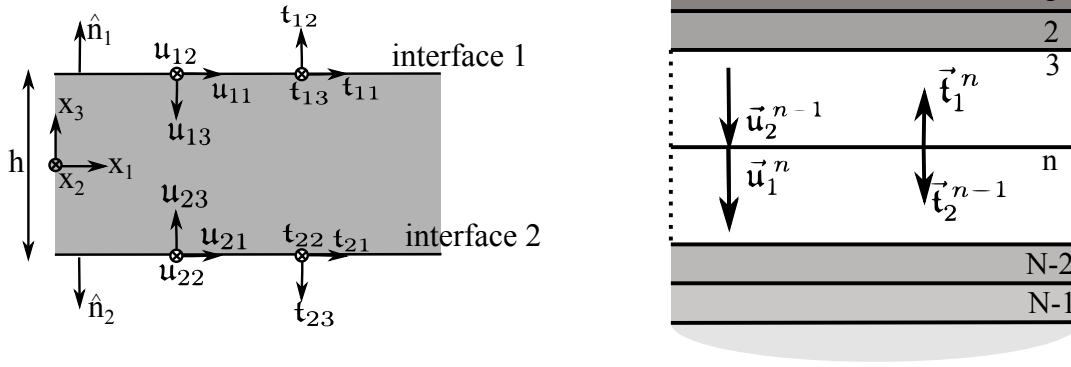
Figure 3.7: *Left: Displacement and tractions on a free layer. The coordinate system is located in the center of the layer and $\hat{n}_1$ and $\hat{n}_2$ are the vectors normal to interface 1 and interface 2, respectively. Right: Horizontally layered medium with $N-1$ layer elements on a half space element.*

Displacement and traction in a single horizontal layer

Next consider a homogeneous, horizontal layer of thickness h where the upper and lower interface are labeled with 1 and 2 following [118], respectively, as in Fig. 3.7, left panel. With the previously derived wavefield (Eq. (3.1.38)), the displacement on interface 1, $\vec{u}_1 = (u_{11}, u_{12}, u_{13})$, and on interface 2, $\vec{u}_2 = (u_{21}, u_{22}, u_{23})$, can be written as

$$
\begin{bmatrix} \vec{u}_1 \\ \vec{u}_2 \end{bmatrix} = \begin{bmatrix} \mathbf{R}_u \mathbf{E}^{-1}(x_3 = \frac{h}{2}) & \mathbf{R}_d \mathbf{E}(x_3 = \frac{h}{2}) \\ \mathbf{R}_u \mathbf{E}^{-1}(x_3 = -\frac{h}{2}) & \mathbf{R}_d \mathbf{E}(x_3 = -\frac{h}{2}) \end{bmatrix} \begin{bmatrix} \vec{a}_u \\ \vec{a}_d \end{bmatrix}, \tag{3.1.40}
$$

where it has been assumed that the center of the coordinate system is in the center of the layer.

The force per unit area on a horizontal interface of the layer, the so called traction, is related to the elements of the stress tensor that correspond to the vector normal to this interface. In this case $\vec{t}_1 = \vec{s}$ is the traction on interface 1 and $\vec{t}_2 = -\vec{s}$ is the traction on interface 2 and with Eq. (3.1.39) this can be written as

$$
\begin{bmatrix} \vec{t}_1 \\ \vec{t}_2 \end{bmatrix} = \begin{bmatrix} -\mathbf{Q}_u \mathbf{E}^{-1}(x_3 = \frac{h}{2}) & \mathbf{Q}_d \mathbf{E}(x_3 = \frac{h}{2})] \\ \mathbf{Q}_u \mathbf{E}^{-1}(x_3 = -\frac{h}{2}) & -\mathbf{Q}_d \mathbf{E}(x_3 = -\frac{h}{2})] \end{bmatrix} \begin{bmatrix} \vec{a}_u \\ \vec{a}_d \end{bmatrix} = \begin{bmatrix} \mathbf{K}_{11} & \mathbf{K}_{12} \\ \mathbf{K}_{21} & \mathbf{K}_{22} \end{bmatrix} \begin{bmatrix} \vec{u}_1 \\ \vec{u}_2 \end{bmatrix}, \text{ with} \tag{3.1.41}
$$

$$
\mathbf{K} = \begin{bmatrix} \mathbf{K}_{11} & \mathbf{K}_{12} \\ \mathbf{K}_{21} & \mathbf{K}_{22} \end{bmatrix}
$$

$$
= \begin{bmatrix} -\mathbf{Q}_u \mathbf{E}^{-1}(x_3 = \frac{h}{2}) & \mathbf{Q}_d \mathbf{E}(x_3 = \frac{h}{2})] \\ \mathbf{Q}_u \mathbf{E}^{-1}(x_3 = -\frac{h}{2}) & -\mathbf{Q}_d \mathbf{E}(x_3 = -\frac{h}{2})] \end{bmatrix} \begin{bmatrix} \mathbf{R}_u \mathbf{E}^{-1}(x_3 = \frac{h}{2}) & \mathbf{R}_d \mathbf{E}(x_3 = \frac{h}{2}) \\ \mathbf{R}_u \mathbf{E}^{-1}(x_3 = -\frac{h}{2}) & \mathbf{R}_d \mathbf{E}(x_3 = -\frac{h}{2}) \end{bmatrix}^{-1},
$$

where in the second step Eq. (3.1.40), solved in terms of the wave amplitudes, has been used and where $\mathbf{K}$ is called the symmetric *stiffness matrix* of the layer. The stiffness matrix of an elastic half-space is obtained for $\vec{a}_d = 0$ and $h \to \infty$.

Displacement and traction in a horizontally multilayered medium

Now consider a system with $N-1$ layers and N interfaces on a half-space (Fig. 3.7, right panel). Following [118], the stiffness matrix of the nth layer is then denoted as

$$\mathbf{K}^n = \begin{bmatrix} K_{n,n} & K_{n,n+2} \\ K_{n+1,n} & K_{n+1,n+1} \end{bmatrix}, \tag{3.1.42}$$

and by overlapping the stiffness matrices of all $N-1$ layers, the total stiffness matrix of the system is of the form

$$\begin{bmatrix} \vec{t}_1 \\ \vec{t}_2 \\ \vec{t}_3 \\ \vdots \\ \vec{t}_N \end{bmatrix} = \begin{bmatrix} \mathbf{K}_{1,1} & \mathbf{K}_{1,2} & 0 & \cdots & 0 \\ \mathbf{K}_{2,1} & \mathbf{K}_{2,2} & \mathbf{K}_{2,3} & \cdots & 0 \\ 0 & \mathbf{K}_{3,2} & \mathbf{K}_{3,3} & \ddots & 0 \\ \vdots & \vdots & \vdots & \ddots & \ddots & \mathbf{K}_{N-1,N} \\ 0 & 0 & \cdots & \mathbf{K}_{N,N-1} & \mathbf{K}_{N,N} \end{bmatrix} \begin{bmatrix} \vec{u}_1 \\ \vec{u}_2 \\ \vec{u}_3 \\ \vdots \\ \vec{u}_N \end{bmatrix}. \tag{3.1.43}$$

For a given traction on an interface, the displacement field is the solution to the matrix inversion problem in Eq. (3.1.43). The traction on the surface represents a source that excites the soil profile. In the context of the dynamic response of a soil to an external source, the displacement field is also referred to as Green's function. In this work we restrict ourselves to harmonic point excitations on the surface of layered soil profiles. Surface point sources allow to model the soil response to anthropogenic sources, which corresponds to seismic noise above 1 Hz that is generated by human activity. Sources at low frequencies are for example microseismic activity, originating from ocean waves interacting with the shore, or earthquakes, which are accompanied by fault slips at great depths below the surface. These type of sources are not of relevance for the analysis of this work. The interested reader can find an overview of modeling techniques for more complex source types and mechanisms in [107].

Even though it is tedious for larger numbers of N, the matrix operation in Eq. (3.1.43) in the frequency-wave number domain may still be derived by hand and a closed-form solution to the above eigenvalue problem may be given. However, the problem further increases in complexity when arbitrary wave propagation in three-dimensional geometries with curved wavefronts are required. Hence, numerical solving tools are required to derive the solution to the eigenvalue problem for a realistic geology.

3.2 Spectral wave analysis

Seismic data are recorded in the time domain, but to extract the spectral components of the seismic field, the analysis is carried out in the frequency domain. To transform the data from the time to the frequency domain, Fourier analysis is used. Since the data points are discrete and to facilitate implementation in software algorithms, Eq. (3.1.31) is modified to the *discrete Fourier transform* (DFT) which maps the elements of the time domain data vector $\vec{x} = (x_0, ..., x_{N-1})$ with N components to its frequency domain counterpart $\vec{y} = (y_0, ...y_{N-1})$ as [120]

$$y_m = \sum_{k=0}^{N-1} x_k \exp(-2\pi i \frac{mk}{N}), \tag{3.2.1}$$

where the index $k = 0, ..., N - 1$ refers to the data points in the time domain vector and $m = 0, .., N - 1$ denotes the index of the data points in the frequency domain representation. As the x_k are real values, the corresponding frequency domain signal is conjugate symmetric as $y_{N-m} = y_m^*$.

The time domain data are sampled with a sampling frequency f_s, which depends on the data acquisition device. According to the Shannon-Nyquist theorem [121], the maximum frequency f_{Ny} that can be resolved equals half of the sampling frequency, so that $f_{Ny} = f_s/2$. So for a signal that is sampled at $100\,\text{Hz}$, information about its spectral content can be obtained up to $50\,\text{Hz}$. By defining the frequency bin width as $f_{res} = \frac{f_s}{N}$, the frequency values of the N data points in Eq. (3.2.1) are

$$f_m = m \cdot f_{res} - f_{Ny}, \tag{3.2.2}$$

which is a vector of N components ranging from $-f_s/2$ to $f_s/2$.

The DFT implicitly assumes that the time domain signal is periodic. Any discontinuity between the first and the last point in the data vector results in a distortion of the signal across the whole frequency domain. To prevent such distortion effects the time domain data are multiplied by a symmetric *window function* before applying the DFT. Window functions typically increase at the beginning of the interval, then peak in the middle and drop again at the end of the interval, hereby suppressing discontinuities at the boundary of the data array. Many different window functions have been defined for a wide variety of purposes, and an extended list can be found in [120]. A common window function is the Hanning window (Fig. 3.8, left panel) which is defined as

$$w_m = \frac{1}{2}[1 - \cos(\frac{2\pi m}{N})], \quad \text{where } m = 0, .., N - 1, \tag{3.2.3}$$

and for normalization purposes the following sums are defined

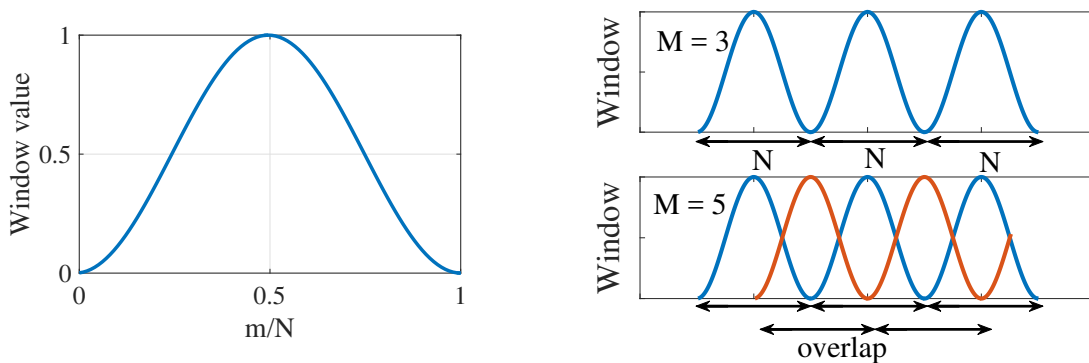$$S_1 \equiv \sum_{m=0}^{N-1} w_m, \quad S_2 \equiv \sum_{m=0}^{N-1} w_m^2. \tag{3.2.4}$$

Figure 3.8: *Left: Hanning window function in the time domain normalized by the number of samples N. Right: If a signal is split into m neighboring segments, information is lost at the boundary of the segments due to the window function (top). To avoid information loss, the M windows are chosen to be overlapping.*

The signal power in the frequency domain is obtained by taking the square of the absolute values of y_m (Eq. (3.2.1)). Normalizing it by the window power, the number of frequency bins N

and the bandwidth f_{res} gives

$$PSD(f_{\tilde{m}} = \tilde{m} f_{res}) = \frac{2 \cdot |y_{\tilde{m}}|^2}{N \cdot f_{res} \cdot S_2} = \frac{2 \cdot |y_{\tilde{m}}|^2}{f_s \cdot S_2},$$
(3.2.5)

where $\tilde{m} = \frac{N-1}{2}, ...N - 1$ is the index that only regards the positive frequency components of Eq. (3.2.2) and where the second, conjugate symmetric side of the spectrum is taken into account by the factor 2 in the nominator. This is called the one-sided *power spectral density* (PSD). It is also common to display the amplitude spectral density (ASD), which is the square root of the PSD.

To reduce the noise fluctuations in a PSD signal, the data array is split into M segments of N samples length. To each segment the window function is applied and the resulting M PSDs are averaged. This allows to reduce the stochastic noise by a factor $1/\sqrt{M}$. If the signal is split into neighboring segments (Fig. 3.8, right panel), information is lost at the boundaries of each segment. To overcome this relic of the window function, the segments are typically chosen to be overlapping. For a Hanning window the standard overlap between two neighboring windows is 50 % .

Coherence and correlation

The nomenclature on this topic is not used consistently in the literature, so in this work the following definitions based on [122,123] will be used. Consider a seismic signal that is measured simultaneously at two different locations, with $X_1(f)$ and $X_2(f)$ being the frequency domain representation of the signal at sensor 1 and 2, respectively. The similarity between the two signals can then be determined via the *frequency domain cross-spectrum* as

$$K_{12}(f) = \frac{\langle X_1(f)X_2^*(f)\rangle}{\sqrt{\langle X_1(f)X_1^*(f)\rangle\langle X_2(f)X_2^*(f)\rangle}},$$
(3.2.6)

where $*$ denotes the complex conjugate operation and $\langle.\rangle$ denotes an average over M data segments. Eq. (3.2.6) is a complex number, where the magnitude $|K_{12}(f)|$ is called the *coherence* and the real part $\mathfrak{Re}(K_{12})$ is called the *correlation*. If two signals are very similar and related to each other by means of a linear transformation the coherence is one, whereas it tends to zero when both signals are completely unrelated. The correlation also contains information about the similarity of the phase of both signals. It is equal to 1 if both signals are in phase and -1 if both signals are completely out of phase. Assuming a seismic signal that is emitted along the line connecting two measurement locations on the surface, the correlation for that signal is given by

$$\mathfrak{Re}(K_{12}) = \cos(\frac{2\pi}{\lambda(f)}\Delta z),$$
(3.2.7)

where $\lambda(f)$ represents the frequency-dependent wavelength and Δz is the distance between the two measurement points. For waves originating uniformly from all azimuth directions θ around the sensor pair, the wavelength that is perceived by that receiver pair is $\lambda = \frac{\lambda(f)}{\cos\theta}$ and the integral over all azimuth angles yields

$$\mathfrak{Re}(K_{12}) = \frac{1}{2\pi}\int_{-\pi}^{\pi}\cos(\frac{2\pi}{\lambda(f)}\Delta z \ \cos\theta)d\theta$$
$$= J_0(\frac{2\pi}{\lambda(f)}\Delta z),$$
(3.2.8)

where J_0 is the zero-order Bessel function of the first kind.

3.3 Seismic model with a complete seismic field

The response of a horizontally layered soil profile to source excitations can be obtained by numerically solving the elastodynamic wave equation. A structural overview of the necessary steps that are required to derive an ambient seismic field model in a specified geology is displayed in Fig. 3.9, left panel. The geology at the detector location can be determined with a seismic study by using a dense sensor array. Beam forming is used to determine the seismic source distribution and the dispersion curve of the subsurface, while seismic inversion is carried out to obtain a horizontally layered subsurface model with velocity, density and damping ratio information (for details see Section 4). This section presents how this geological information is used to obtain a model for a seismic field with use of the full solution of the elastodynamic wave equation.
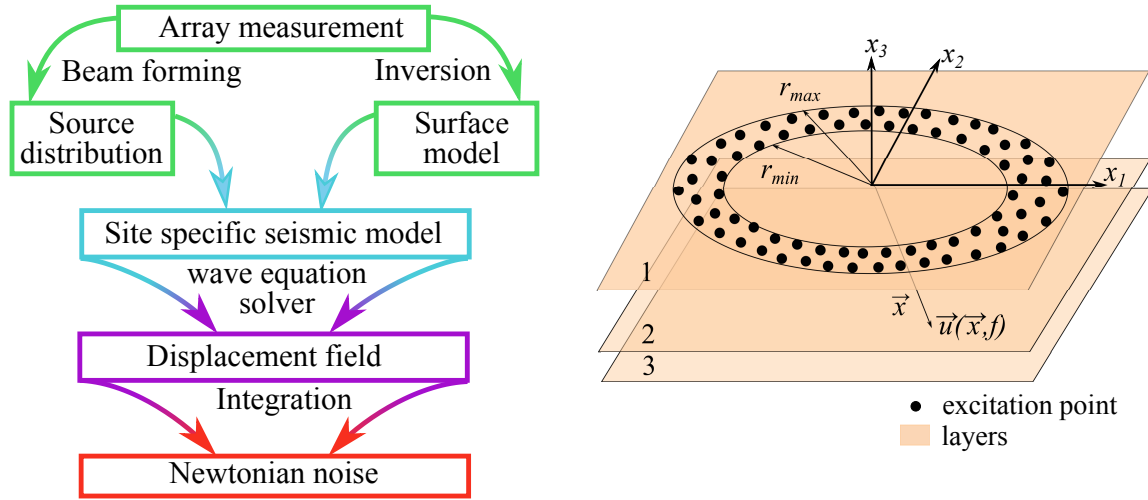

Figure 3.9: *Left: The lithology and source distribution at the site are determined with seismic sensor array measurements (green). Solving the elastodynamic wave equation for the derived seismic model (blue) results in a seismic displacement field that is characteristic for the site (purple). Integrating over the seismic displacements allows to calculate the Newtonian noise on a test mass located in this wave field (red). Right: Schematic layout of the model for an ambient seismic field. Excitation points, where the soil is horizontally and vertically excited, are placed in a ring around a region where the ambient seismic field is calculated.*

The soil response to source excitations is obtained by numerically solving the elastodynamic wave equation with the Matlab Elastodynamics toolbox [117, 119]. The response is a three-dimensional vector field denoted as $\vec{u}(\vec{x}, f) = (u_1(\vec{x}, f), u_2(\vec{x}, f), u_3(\vec{x}, f))$ (Fig. 3.10). It represents the complex amplitude of the seismic displacement at a receiver location $\vec{x}$ to a source oscillating with frequency f. To model an ambient seismic field the soil is vertically excited at N excitation points, which are located within a ring of r_{min} and r_{max} from the center of the geometry (Fig. 3.9, right panel).

The response at the receiver location $\vec{x}$ to the nth-source is denoted as $\vec{u}_n(\vec{x}, f)$. The default strength of a source is 1 N. Due to the linear relationship between traction and displacement (see Eq. (3.1.43)), increasing the source strength directly leads to an increase of the displacement magnitude by the same factor. In a realistic geology, the strength of the sources depends on their cardinal direction. It is for example possible, that source excitations from the northern direction are dominant across the whole frequency band. To take this directional dependence into consideration, a *relative scaling factor* $\tilde{m}_n(f)$ is introduced, where the subscript indicates
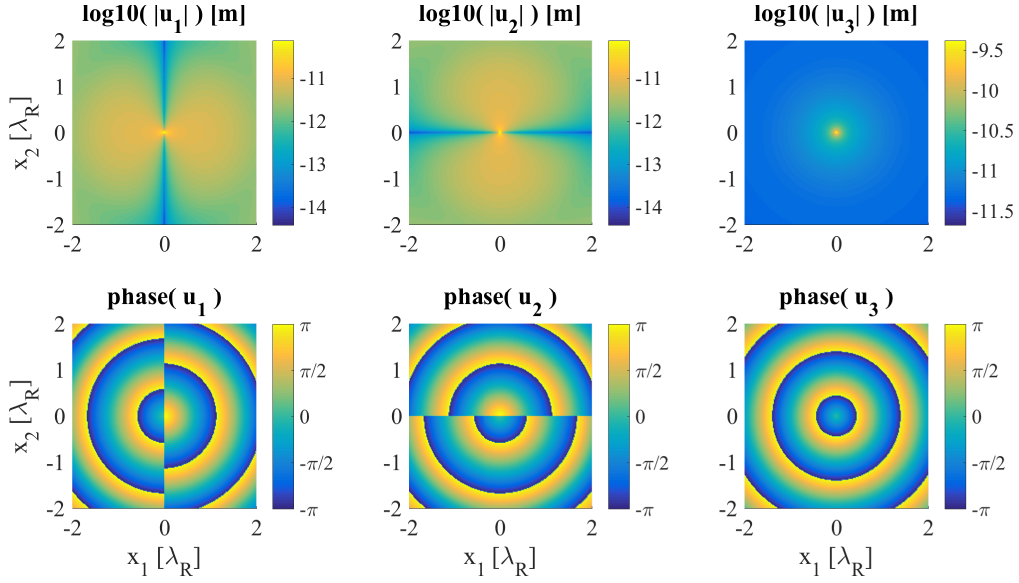
Figure 3.10: *Amplitude, top row, and phase, bottom row, of the three displacement components from a vertical excitation of a half-space in the center of the geometry, where the phase indicates the direction of the displacement. Along the x_1-axis (x_2-axis) the horizontal displacement is purely in the x_1-direction (x_2-direction) and at any other point the radial displacement is a superposition of u_1 and u_2.*

that the scaling factor corresponds to the nth-source. The value of the relative scaling factor is derived from the beam power, a quantity that can be measured with a seismic sensor array. It appoints the main energy content of a seismic field to a cardinal direction (see Section 4.2). The response of the soil to a force $F(f) = \tilde{m}_n^{1/2}(f)$ is then calculated by multiplying the power of the default response $|\vec{u}_n(\vec{x}, f)|^2$ of the nth-source by the relative scaling factor $\tilde{m}_n(f)$.

All sources are assumed to act as incoherent noise sources, which means that for the total ambient seismic field at $\vec{x}$ the individual responses are summed quadratically as

$$|u_i(\vec{x}, f)|^2 = \sum_{n=1}^{N} \tilde{m}_n(f) \cdot |u_{i,n}(\vec{x}, f)|^2 \; [\text{m}^2], \tag{3.3.1}$$

where the index $i = 1, 2, 3$ indicates the ith component of the displacement vector. Modeling the seismic field as a coherent sum is in principle possible as well. However, the seismic field from a coherent sum would rather describe a single, complicated soil excitation, whereas the incoherent sum attributes a transient, individual displacement field from each noise source.

Using the fact that the squared absolute value of the displacement $|u_i(\vec{x}, f)|^2$ is proportional to the PSD, an *absolute scaling factor* $m(f)$ (in units $[1/\text{Hz}]$) can be introduced as the proportionality constant. The absolute scaling factor ensures that the strength of the sources is increased equally such that the resulting simulated PSD is equivalent to the measured PSD as

$$\text{PSD}_i(\vec{x}, f) = m(f) \cdot |u_i(\vec{x}, f)|^2 \; [\text{m}^2/\text{Hz}]. \tag{3.3.2}$$

For a specific geology, the absolute scaling factor can be obtained by solving Eq. (3.3.2) for a PSD that has been measured for example at the surface of the site. The total, scaled wave field is then obtained by multiplying the displacements at all locations with the obtained scaling factor.

3.4 Newtonian noise in a horizontally layered geology

When the seismic displacement field is known at all points of a geology, it can be used to calculate Newtonian noise on a test mass of a gravitational wave detector embedded in this geology. Newtonian noise is the motion of the test mass due to Newtonian interaction with seismically induced density fluctuations in the soil surrounding the detector. To derive the connection between seismic displacement and density fluctuation, first consider a small, cubic volume element of width w in a homogeneous medium where a displacement field moves the volume element at $\vec{x}$ by $\vec{u}(\vec{x}, f) = (u_1(\vec{x}, f), u_2(\vec{x}, f), u_3(\vec{x}, f))$ (Fig. 3.11, left panel). The resulting density fluctuations are assumed to be much smaller than the displacements such that an unperturbed, uniform density ρ_0 can be assumed to first order across the medium. For a displacement only in the x_1-direction, the total change in mass at the location of the original volume element is

$$\delta m_1 = m_{in} - m_{out} = -\rho_0 w^2 \big(u_1(x_1 + w, x_2, x_3) - u_1(x_1, x_2, x_3) \big), \qquad (3.4.1)$$

where $m_{in} = \rho_0 w^2 u_1(x_1, x_2, x_3)$ represents the mass that flows into and $m_{out} = \rho_0 w^2 u_1(x_1 + w, x_2, x_3)$ the mass that flows out of the original location of the volume element. For an infinitesimal small volume element the density fluctuation $\delta \rho_1 = \frac{\delta m_1}{w^3}$ from the displacement in the x_1-direction can then be expressed as

$$\delta \rho_1 = -\rho_0 \lim_{w \to 0} \frac{u_1(x_1 + w, x_2, x_3) - u_1(x_1, x_2, x_3)}{w} = -\rho_0 \frac{\partial u_1}{\partial x_1}, \qquad (3.4.2)$$

where the partial derivative has been defined as

$$\frac{\partial f(x, y)}{\partial x} = \lim_{a \to 0} \frac{f(x + a, y) - f(x, y)}{a}. \qquad (3.4.3)$$

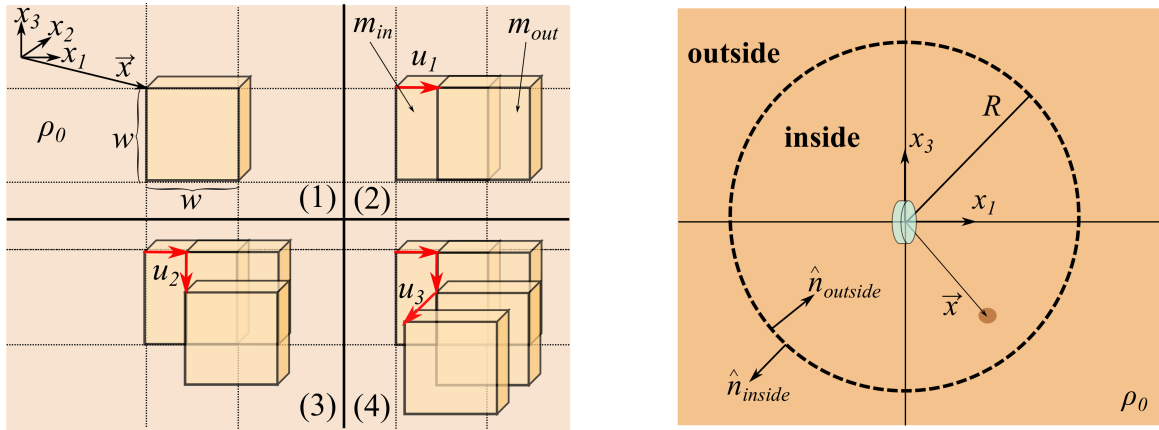**Figure 3.11:** *Left: A cubic volume element with width w at location $\vec{x}$ in a medium of unperturbed density ρ_0 is displaced with $\vec{u}(\vec{x}, f) = (u_1, u_2, u_3)$. Right: Sketch of a test mass fully embedded in an unbound, homogeneous medium with unperturbed density ρ_0, where the test mass is located at the center of the coordinate frame with the x_2-axis pointing into the drawing. The integration area is separated in an area inside and outside a volume that is defined by the maximum integration radius R. The normal vectors on the interface that separates both areas are $\hat{n}_{inside}$ and $\hat{n}_{outside}$ and they are pointing outwards with respect to the part of the volume they correspond to.*

The sum of the individual fluctuations gives the total density fluctuation due to the displacement $\vec{u}(\vec{x}, f)$ as

$$
\begin{aligned}
\delta\rho(\vec{x}, f) &= \delta\rho_1 + \delta\rho_2 + \delta\rho_3 \\
&= -\rho_0\left(\frac{\partial u_1(\vec{x}, f)}{\partial x_1} + \frac{\partial u_2(\vec{x}, f)}{\partial x_2} + \frac{\partial u_3(\vec{x}, f)}{\partial x_3}\right) \\
&= -\rho_0\, \nabla \cdot \vec{u}(\vec{x}, f),
\end{aligned}
\tag{3.4.4}
$$

where ∇ is the Nabla operator. This equation describes density fluctuations as a result of seismic motion and it is the basis of the following Newtonian noise derivation.

Newtonian acceleration in an unbound, homogeneous medium

Consider a test mass of a gravitational wave detector that is fully embedded in an unbound, homogeneous medium with unperturbed density ρ_0, where the center of the coordinate grid is placed at the location of the test mass (Fig. 3.11, right panel). The acceleration of the test mass due to density fluctuation $\delta\rho(\vec{x}, f)$ can then be obtained according to Newton's second law by integrating over the volume as

$$
\delta\vec{a}(f) = G\int_V \delta\rho(\vec{x}, f)\frac{\vec{x}}{|\vec{x}|^3}\, dV,
\tag{3.4.5}
$$

where G represents the gravitational constant and $\vec{x}$ the vector pointing from the test mass in the direction of the density fluctuation. Substituting $\vec{k}(\vec{x}) \equiv \frac{\vec{x}}{|\vec{x}|^3}$ and with Eq. (3.4.4) the Newtonian acceleration of the test mass becomes

$$
\begin{aligned}
\delta\vec{a}(f) &= -G\int_V \rho_0\big(\nabla \cdot \vec{u}(\vec{x}, f)\big)\,\vec{k}(\vec{x})\, dV \\
&= -G\left(\int_V \rho_0\nabla \cdot \big(\vec{u}\,\vec{k}\big)\, dV - \int_V \rho_0\big(\vec{u}\cdot\nabla\big)\vec{k}\, dV\right) \\
&= -G\left(\int_S \rho_0 u_1 n_1\vec{k}\, dS_{23} + \int_S \rho_0(\vec{x})u_2 n_2\vec{k}\, dS_{13} + \int_S \rho_0(\vec{x})u_3 n_3\vec{k}\, dS_{12}\right. \\
&\qquad \left. - \int_V \rho_0\big(\frac{\partial\vec{k}}{\partial x_1}u_1 + \frac{\partial\vec{k}}{\partial x_2}u_2 + \frac{\partial\vec{k}}{\partial x_3}u_3\big)\, dV\right) \\
&= G\int_V \rho_0\big(\vec{u}\cdot\nabla\big)\vec{k}\, dV - G\int_S \rho_0\big(\vec{u}\cdot\hat{n}_S\big)\vec{k}\, dS,
\end{aligned}
\tag{3.4.6}
$$

where for readability the arguments of the fields have been suppressed. In the third line Gauss's divergence theorem converts the volume to a surface integration and the integrals are given in Cartesian representation, where dS_{ij} refers to the surface integral across the $x_i x_j$-planes. In the last step the integral has been reformulated in terms of a coordinate independent representation, where $\hat{n}_S = (n_1, n_2, n_3)$ is the outward pointing vector normal to the surface that encloses the integration volume.

Next the integrals can be split into a region outside and inside a maximum integration area, that are separated by the integration radius R. The maximum integration radius R is defined such that 90 % of the Newtonian noise is derived from the spherical volume enclosed within this

radius. The acceleration of the test mass in the unbound, homogeneous medium then becomes

$$\delta\vec{a}(f) = G\Bigg(\int_V \rho_0\big(\vec{u}\cdot\nabla\big)\vec{k}\,dV_{inside} - \int_S \rho_0\big(\vec{u}\cdot\hat{n}_{inside}\big)\vec{k}\,dS$$
$$+ \int_V \rho_0\big(\vec{u}\cdot\nabla\big)\vec{k}\,dV_{outside} - \int_S \rho_0\big(\vec{u}\cdot\hat{n}_{outside}\big)\vec{k}\,dS\Bigg)$$
$$= G\int_V \rho_0\big(\vec{u}\cdot\nabla\big)\vec{k}\,dV_{inside}, \tag{3.4.7}$$

where after the second step only the volume integral enclosed by R remains, because the contribution of the volume outside R to Newtonian noise is negligible. The surface integrals represent the mass flowing in and out of the integration volume, and since $-\hat{n}_{outside} = \hat{n}_{inside}$ both contributions cancel each other if the medium is continuous with constant density ρ_0. This means that in an unbound, homogeneous medium Newtonian noise is generated only by density fluctuations within the integration volume.

Newtonian noise in a layered medium

Consider now a test mass located at a depth h in a realistic, layered geology. It is instructive to first consider a geology with $M = 2$ layers of density ρ_m as depicted in Fig. 3.12. The Newtonian acceleration can then be derived from the contributions of the individual layers according to Eq. (3.4.6), where the part of the surface integral where seismic displacement occurs within the medium of the same density cancels out as derived in Eq. (3.4.7). The remaining part of the surface integral corresponds then to the interfaces between the layers and the resulting Newtonian acceleration can be expressed as

$$\delta\vec{a}(f) = G\Bigg(\int_V \rho_1\big(\vec{u}\cdot\nabla\big)\vec{k}\,dV_1 - \int_S \rho_1\big(\vec{u}\cdot\hat{n}_{1,up}\big)\vec{k}\,dS_1 - \int_S \rho_1\big(\vec{u}\cdot\hat{n}_{1,down}\big)\vec{k}\,dS_1$$
$$+ \int_V \rho_2\big(\vec{u}\cdot\nabla\big)\vec{k}\,dV_2 - \int_S \rho_2\big(\vec{u}\cdot\hat{n}_{2,up}\big)\vec{k}\,dS_2\Bigg)$$
$$= \sum_{m=1}^{M} G\Bigg(\int_V \rho_m\big(\vec{u}\cdot\nabla\big)\vec{k}\,dV_m + (\rho_{m-1}-\rho_m)\int_S \big(\vec{u}\cdot\hat{n}_m\big)\vec{k}\,dS_m\Bigg), \tag{3.4.8}$$

where the volume and surface integral of the mth layer are represented by dV_m and dS_m, and where $\hat{n}_{m+1,up} = -\hat{n}_{m,down} = \hat{n}_{m+1}$ holds for the normal vectors on the interface between the
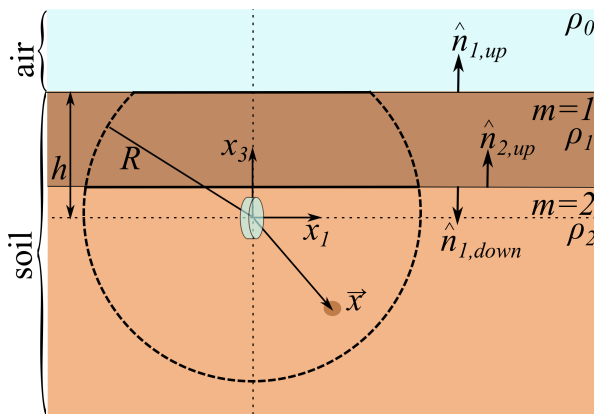

Figure 3.12: *Sketch of a test mass embedded at a depth h in a medium with $M = 2$ layers, where the density of each layer is indicated with ρ_m. Air has a density of $\rho_0 = 0$ and is not counted as layer. The vectors normal to the horizontal interfaces of the mth layer are indicated with $\hat{n}_{m,up}$ and $\hat{n}_{m,down}$. The bottommost layer is unbound in the downward direction and therefore the normal vector $\hat{n}_{M,down}$ is not defined.*

m^{th} and the $(m + 1)^{th}$ layer. The last line of Eq. (3.4.8) is then the general expression for the Newtonian acceleration of a test mass in a horizontally layered medium with M layers. Due to the dependence of Eq. (3.4.8) on the site-specific subsurface geology and the employment of a seismic field that depends on the local seismic source distribution and that encompasses the full solution of the wave equation in the characteristic geology (see Section 3.3), the Newtonian noise derived from this approach will be referred to as *site-based Newtonian noise*.

Following the approach in [45] the derivatives of the elements of the vector $\vec{k} = \frac{\vec{x}}{|\vec{x}|^3}$ can be expressed as

$$\frac{\partial k_i}{\partial x_j} = \frac{1}{|\vec{x}|^5}(\delta_{ij}|\vec{x}|^2 - 3x_i x_j), \qquad (3.4.9)$$

where δ_{ij} is the Kronecker delta, which allows to reformulate the volume integral of the mth layer in Eq. (3.4.8) as

$$\delta\vec{a}_{V_m}(f) = G \int_V \rho_m \frac{1}{|\vec{x}|^5} \begin{bmatrix} |\vec{x}|^2 - 3x_1^2 & -3x_1 x_2 & -3x_1 x_3 \\ -3x_2 x_1 & |\vec{x}|^2 - 3x_2^2 & -3x_2 x_3 \\ -3x_3 x_1 & -3x_3 x_2 & |\vec{x}|^2 - 3x_3^2 \end{bmatrix} \begin{bmatrix} u_1(\vec{x}, f) \\ u_2(\vec{x}, f) \\ u_3(\vec{x}, f) \end{bmatrix} dV_m, \quad (3.4.10)$$

where a Cartesian representation has been chosen. Note that in special cases, such as a test mass surrounded by a spherical cavern on the surface of a homogeneous half-space surface with a constant displacement in only one horizontal direction, the volume contribution vanishes. This is however not true when the medium is not homogeneous or the mirror is surrounded by an asymmetric cavern. In this case constant displacements leads to an acceleration of the test mass that does not necessarily have to be in the direction of the displacement.

The Newtonian acceleration of a test mass due to a seismic field from N incoherent sources is calculated equivalently to Eq. (3.3.2). First the Newtonian acceleration is derived from the complex displacement field of each source individually (Eq. (3.4.8)), then these contributions are summed incoherently. By taking into account the previously derived relative and absolute scaling factors the ith component of the *Newtonian noise* can be written as

$$\delta a_{i,NN}(f) = m(f) \cdot \sum_{n=1}^{N} \tilde{m}_n(f) \cdot |\delta a_{i,NN}^{(n)}(f)|^2 \; [(\mathrm{m/s}^2)^2/\mathrm{Hz}]. \qquad (3.4.11)$$

In a broader sense, Newtonian noise is referred to as the output of a gravitational wave detector due to the seismically induced Newtonian acceleration at all four test masses. Assume a detector with distance L between two test masses. An interferometer arm is typically much longer than the seismic wavelengths for frequencies above $2\,\mathrm{Hz}$. This implies that the forces on the test masses are uncorrelated and the total difference in separation is obtained by a sum over the individual test mass motions in power. The resulting Newtonian (strain) noise is then

$$h_{NN}(f) = \frac{1}{L(2\pi f)^2} \sqrt{\sum_{n=1}^{4} \delta a_{i,NN}^{(n)}(f)^2}, \qquad (3.4.12)$$

where the index n labels the test masses. As the horizontal test mass motion parallel to the detector arms is of relevance for Newtonian noise, the index $i \in \{1, 2\}$ labels the corresponding horizontal component of the Newtonian acceleration vector.

3.5 Going beyond analytical Newtonian noise models

Analytical surface models

Modeling Newtonian noise requires a description of the local seismic field and geology. The first model for Newtonian noise has been derived by Saulson in 1984 [124] and it is used until today for Newtonian noise estimates in the design sensitivity of gravitational wave detectors [52, 66]. Since numerical solving tools were not available at that time, Saulson based his model on an analytical derivation assuming a detector on the surface and a half-space geology with density ρ. Furthermore, it is assumed that the seismic field consists of independent regions, that are coherent across a length of $\lambda/2$, where λ is the wavelength. It is assumed that these regions fluctuate independently of each other, and that the Newtonian acceleration of the test mass can be formulated as an incoherent sum over the contribution from the individual patches. The horizontal component of the Newtonian acceleration parallel to the detector arm in the x_1-direction is then derived as

$$|\delta a_1(f)|^2 = \sum_i \left| \frac{F_{i,1}}{M} \right|^2 = G^2 \sum_i \left| \Delta m_i(f) \frac{\cos \theta_i}{|\vec{r}_i|^2} \right|^2, \tag{3.5.1}$$

where $F_{i,1}$ represents the horizontal component of the force between the ith volume element at location $\vec{r}_i$ and the test mass with mass M, Δm_i is the mass fluctuation of the volume element, θ_i the angle between the volume element and the detector arm and G the gravitational constant. To facilitate the sum, it is converted to an integral where a lower cutoff radius of $\lambda/4$ is introduced to avoid a singularity as $|\vec{r}_i|$ approaches zero (see Appendix C for a summary of the derivation). Next, it is assumed that the fluctuation of mass $\delta m_i(f)$ in the volume element is directly proportional to the displacement amplitude $|\Delta X(f)|$ of the coherent region, which is in units $[\text{m}/\sqrt{\text{Hz}}]$ and a quantity that is measurable by seismometers. For simplicity it is assumed that the amplitude of the displacement is uniform across the entire half-space surrounding the test mass. The expression for the horizontal displacement Newtonian noise $|\delta x_1(f)|^2$ of four independent test masses can then be derived as

$$\begin{aligned} |\delta x_1(f)|^2 &= \frac{|\delta a_1(f)|^2}{(2\pi f)^4} \\ &= \frac{16\pi^2}{3} \frac{G^2 \rho^2}{(2\pi f)^4} |\Delta X(f)|^2 \ \ [\text{m}^2/\text{Hz}]. \end{aligned} \tag{3.5.2}$$

It is important to understand that Saulson's result in Eq. (3.5.2) is only valid for a surface detector where the integration is carried out over a half-space, where no explicit assumption on a cavern shape, geology, source distribution, seismic waves, possible mode conversions, damping and amplitude attenuation with distance or depth have been made. Moreover, it needs to be understood that the cutoff condition of $\lambda/4$ leads to the factor $\frac{16\pi^2}{3}$ in Eq. (3.5.2). If the cutoff condition would be changed for example to $\lambda/2$, the factor in Eq. (3.5.2) would change to $\frac{2\pi^2}{3}$ and a smaller Newtonian noise level would be obtained. Note that this model has been used for Newtonian noise estimates in the Advanced Virgo design sensitivity curve [52, 53] and in the conceptual design study for the underground Einstein Telescope detector [66]. Moreover, numerous scientific papers have been written where event rates have been based on this Einstein Telescope sensitivity, see [125] and references within.

In an attempt to overcome some of the simplifications in the wavefield and geology in Eq. (3.5.2), the analytical model has been expanded by assuming plane Rayleigh waves, contributions from bulk and surface of a half-space and dispersive soil properties [126–128]. Combining these methods leads to an expression for the horizontal displacement Newtonian noise of a surface detector as [129]

$$|\delta x_1(f)|^2 = \beta^2 4\pi^2 \frac{G^2\rho^2}{(2\pi f)^4}|\Delta X(f)|^2 e^{-\frac{2\pi h}{\lambda}},$$

(3.5.3)

where h is the height of the test mass above ground and the factor $\beta < 1$ is related to the dispersive properties of the detector geology. For the geology at the LIGO detectors, β has been estimated to be of the order $\beta \approx 0.35 - 0.6$ for quiet and $\beta \approx 0.15 - 1.4$ for noisy times [128].

All these models are confined to surface waves, since no detailed geological model of the subsurface at the detector sites nor a realistic distribution of noise sources and their spectral content was at hand. Together with finite element models of underground seismic fields in homogeneous media [45, 130], early studies stressed the necessity of a detailed seismic model, including the full solutions to the elastodynamic wave equation for a realistic geology of the detector site.

Site-based Newtonian noise model

To overcome the computational simplifications and assumptions about the seismic field and geology that were necessary to analytically derive the Newtonian noise expression in Eq. (3.5.2), Newtonian noise in this work is derived from Newton's second law, where the acceleration of a test mass is calculated from the integral over the density fluctuations across the entire volume as

$$\delta \vec{a}(f) = G \int_V \frac{\delta\rho(\vec{r}, f)}{|\vec{r}|^2}\hat{r} \, dV,$$

(3.5.4)

where density fluctuations $\delta\rho(\vec{r}, f)$ are connected to the seismic displacement through the continuity equation (see Eq. (3.4.4)). The seismic displacement is derived from the full solution of the elastodynamic wave equation in a detector-specific horizontal geology that takes the local noise source distribution into account (see Section 3.3) and in the following it is therefore referred to as *site-based Newtonian noise*. In its final expression the site-base Newtonian noise incorporates the coherent sum and difference of contributions from the bulk volume and the interfaces between media with different material properties (see Eq. (3.4.8)). Furthermore, the individual integrals are carried out with a Gaussian quadrature algorithm, a numerical integration method (see Appendix B).

Comparison of our site-based Newtonian noise to predictions from the analytical models for a constant wave field

A qualitative comparison between the analytical approach given by Eq. (3.5.2) and our site-based Newtonian noise is possible and assumes the same homogeneous half-space geology, lower cutoff radius and displacement field. For this comparison, a homogeneous half-space with a density of $\rho = 2000 \frac{\text{kg}}{\text{m}^3}$, a Rayleigh wave speed of $v_R = 280 \frac{\text{m}}{\text{s}}$ and a constant, horizontal displacement of $1 \frac{\text{nm}}{\sqrt{\text{Hz}}}$ is assumed. Following Saulson's model, a minimum integration radius

of $\lambda_R/4$ has been used in Eq. (3.5.4), which corresponds to 280 m at 1 Hz and to 28 m at 10 Hz in this example.

First, the test mass in our site-based Newtonian noise is assumed to be at a height of $h = 0$ m, the same as in the analytical approach. For our numerical model the only contribution to Newtonian noise originates from the spherical soil-to-air interface. The contribution from the volume is zero, because of the absence of a density gradient in the horizontal direction of the half-space. With the above specified parameters and Eq. (3.4.8), the displacement power of the test mass can be analytically derived and deviates from Eq. (3.5.2) by a factor 3 (see Fig. 3.13 (a)). Note that this disagreement is coincidental and would not occur for a different cutoff condition. The prefactor attributed to the cutoff in the analytical approach leads to an increasing Newtonian noise for a decreasing cutoff radius and is singular for a cutoff radius of zero (see Eq. (C.4)). In contrast, the surface integral in our site-based approach represents a displacement flux through the spherical interface. As the integration radius decreases, the amount of mass being displaced on the interface decreases as well and as a result the site-based Newtonian noise is well behaved and the same for different cutoff conditions for a constant, horizontal displacement. Another contributing factor may originate from the fact that in the site-based approach, the cavern is taken into account by adjusting the integration bounds of the integral. However, the solving software is limited to a strictly horizontal soil profile, which does not allow to model seismic displacements between soil and air on arbitrary cavern walls. As a result, the Newtonian noise from Eq. (3.5.2) may be considered as upper bound of the Newtonian noise of a surface test mass under the given seismic conditions, which qualitatively agrees with the Newtonian noise from the site-based approach.

As the numerical evaluation of the integral of our site-based Newtonian noise allows for a minimum integration bound of zero, it is possible to evaluate the same integral without the lower cutoff radius. For a homogeneous, unbound medium without discontinuity in the horizontal direction, that is displaced horizontally, each moving volume element is replaced by a volume element with identical density and thus the total Newtonian noise of a test mass at $h = 0$ m vanishes. The same argument holds if the test mass is located above ground; for a pure horizontal displacement of the soil, the site-based Newtonian noise vanishes. Note that in both cases, the
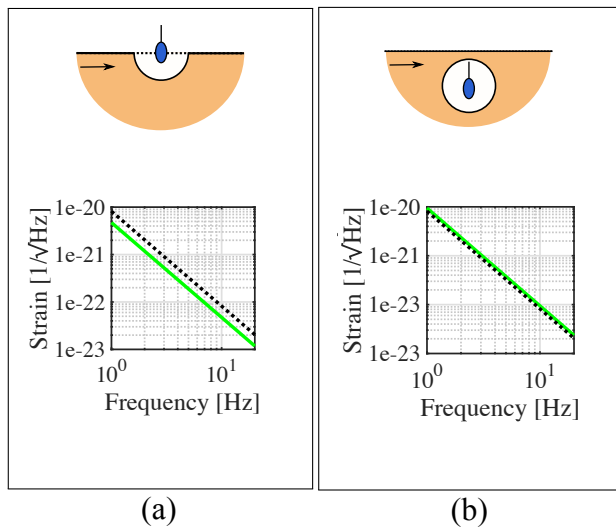

Figure 3.13: *The Newtonian noise derived with Saulson's analytical model, with a test mass height of $h = 0$ m and a frequency dependent cutoff radius of $\lambda/4$, is depicted in dashed black in both bottom panels. Our site-based Newtonian noise is depicted in green. In panel (a) it differs by a factor $\sqrt{3}$ from the Newtonian noise from the analytical model for a test mass height of $h = 0$ m and the same frequency dependent cutoff radius. In panel (b), the site-based Newtonian noise for a a test mass at arbitrary depth and a cavern radius of $\lambda/4$ is a factor two above the green curve in panel (a).*

Newtonian noise prediction from the analytical approach would diverge towards infinity, when such a variable cutoff condition would be applied.

Finally, the test mass is located underground at a depth of 500 m with a frequency dependent cavern radius of $\lambda/4$ (Fig. 3.13 (b)). As before, the contribution from the volume vanishes and only the spherical interface between soil and air contributes to the site-based Newtonian noise. This means that in that case the site-based Newtonian noise is the same for any arbitrary test mass depth when the cavern is spherical. The surface integral is a representation of the displacement flux through the surface and due to the absence of a density gradient, this surface integral is equal for all cavern radii. The site-based Newtonian noise from the underground cavern is then a factor 2 larger than what is expected for a hemispherical cavern on the surface.

Introducing realistic seismic fields   Previously, constant horizontal displacement in a half-space geology was assumed. However, realistic seismic displacement is not constant in depth or distance.

The first step towards the evaluation of our site-based Newtonian noise with realistic seismic fields is to introduce the seismic displacement from a plane Rayleigh wave according to Eq. (3.1.26). The amplitudes of the Rayleigh waves are scaled such that the horizontal displacement on the surface amounts to $1 \; \frac{\text{nm}}{\sqrt{\text{Hz}}}$. The geology model is as previously assumed to be a half-space with density $\rho = 2000 \; \frac{\text{kg}}{\text{m}^3}$ and has a Rayleigh wave speed of $v_R = 280 \; \frac{\text{m}}{\text{s}}$. To facilitate a comparison to the analytical approach, the test mass is located at $h = 0$ m and a frequency dependent, lower cutoff radius of $\lambda_R/4$ is used. The numerical integral is carried out up to a maximum radius of $2\lambda_R$, which is an integration range that comprises more than 90 % of the Newtonian noise on the test mass. For concrete examples of the determination of the integration radius, the reader is referred to Section 5.3 and Section 6.3.

The density gradient from the plane Rayleigh waves across the volume in horizontal and vertical direction results in a contribution of the volume and the soil-to-air interface to our site-based Newtonian noise. The volume contribution dominates the contribution from the interface (see Fig. 3.14 (a)). Since the amplitudes of the Rayleigh waves attenuate quickly with depth, the corresponding Newtonian noise is below Saulson's analytical expectation, which significantly overestimates seismic amplitudes underground.

Next, Newtonian noise is derived from a seismic field that is the response of a vertical excitation of the half-space. The site-based Newtonian noise expression in Eq. (3.4.11) is based on the incoherent sum of Newtonian noise from a large number of sources at various distances and angles with respect to the test mass. As the Newtonian noise on the test mass is calculated individually for each source, it is sufficient for the simplicity of this qualitative comparison to only consider Newtonian noise from excitations with a single source. The seismic field is then derived from the soil response from a vertical source and it therefore comprises surface and body waves, as well as attenuation of seismic amplitudes with distance from the source. As a result, the exact composition of the seismic field depends on the distance from the source.

If the source is at large distance, that is more than $7\lambda_R$ from the integration area, then body waves have mostly attenuated and the surface field consists dominantly of Rayleigh waves (see Fig. 3.14 (b)). Even though the seismic field at the test mass location consists mostly of Rayleigh waves, the amplitudes attenuate with $1/r$ as a function of distance r from the source in the entire integration area. Individual volume and interface Newtonian noise contributions are almost equivalent and are comparable to the analytical expectation. However, they are added coherently (see Eq. (3.4.8)) and our resulting site-based Newtonian noise is less than what is derived for a
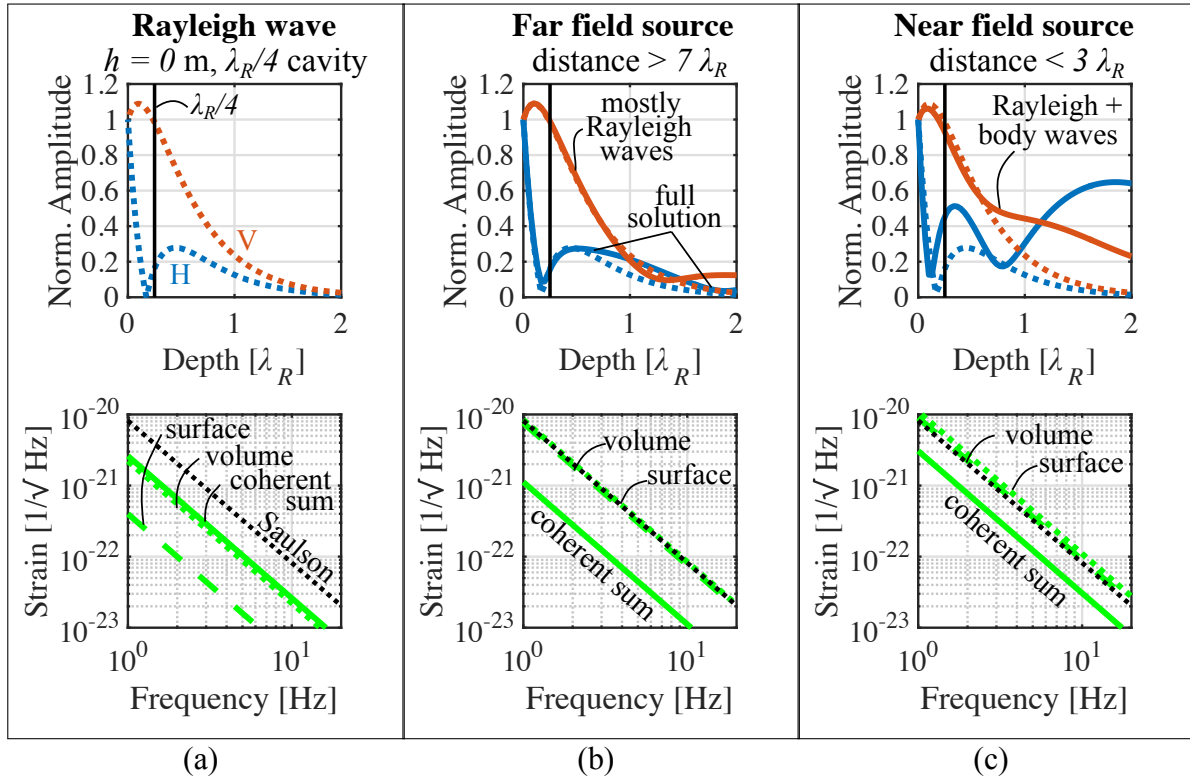
Figure 3.14: *The top panel of each column displays the horizontal (blue) and vertical (red) amplitudes of the seismic field, where the dotted curves indicate Rayleigh wave displacement and the full curves the seismic field from the full solution of the wave equation at $3\,\mathrm{Hz}$. The vertical black line indicates $\lambda_R/4$. The bottom panel displays Saulson's analytical expectation by a black dashed curve and the horizontal, site-based Newtonian noise in green, where the volume contribution is represented by a dotted curve, the interface contribution by a dashed curve and the coherent sum by a full curve. Furthermore, the test mass is at $h = 0$ m and a cutoff radius of $\lambda_R/4$ is assumed. (a) For a seismic field that is comprised of plane Rayleigh waves, the contribution of the volume dominates our site-based Newtonian noise. It is less than the analytical expectation due to the attenuation of wave amplitudes with depth. (b) For a seismic field from a far field source excitation, the seismic field consists mainly of Rayleigh waves. As these waves also attenuate with distance from the source, our site-based Newtonian noise decreases with respect to the seismic field from a plane Rayleigh wave. Note that even though the individual volume and surface contributions are in the range of the analytical expectation, they are added coherently and thus can lead to a reduction in Newtonian noise. (c) For a seismic field from a near field source the seismic field comprises a superposition of body and surface waves. This leads to an increase of subsurface amplitudes in the seismic field and thus to a higher site-based Newtonian noise than from a far away source.*

plane Rayleigh wave.

A source close to the integration area, that is within a distance of $3\lambda_R$, leads to a more complex wave field with interfering body and Rayleigh waves and thus to higher subsurface amplitudes compared to the field from a source at large distance (Fig. 3.14 (c)). These higher amplitudes increase the individual contributions of the volume and interface to Newtonian noise. Even though they are added coherently, our site-based Newtonian noise from the nearby source is higher than the expectation from the far excitation due to the additional contribution of body

waves. The exact level of Newtonian noise is dependent on the distance between source and test mass position.

Varying the test mass height in a realistic seismic field   It is of interest to qualitatively study site-based Newtonian noise depending on the height of the test mass with a fixed cavern radius in a geology that comprises a wave field with body and surface waves. For this comparison, a half-space geology with density $\rho = 2000 \ \frac{\text{kg}}{\text{m}^3}$ and Rayleigh wave speed $v_R = 280 \ \frac{\text{m}}{\text{s}}$ is assumed. The seismic field is obtained from a vertical excitation at $5\lambda_R$ from the test mass. The resulting displacement allows Rayleigh waves to be dominant on the surface, but also includes a significant contribution of body waves at shallow depths. The strength of the source is chosen such, that the horizontal displacement at the center of the integration area is $1 \ \frac{\text{nm}}{\sqrt{\text{Hz}}}$ across the whole frequency range.
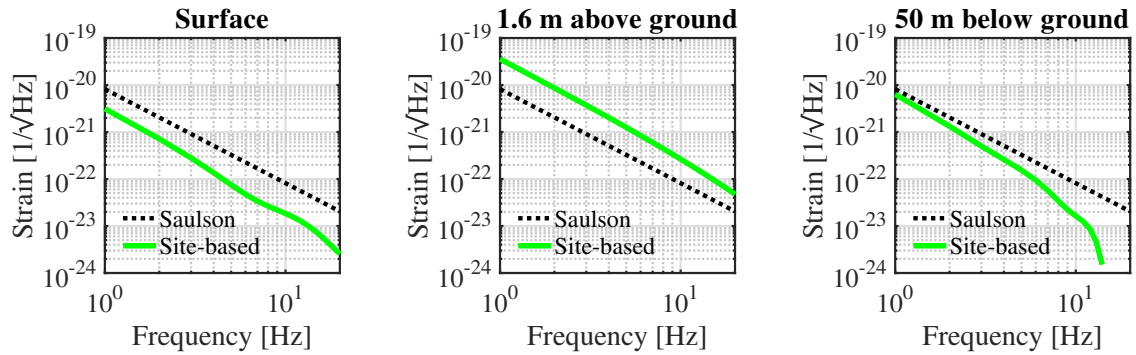

Figure 3.15: *Newtonian noise from Saulson's analytical model for $h = 0$ and $\lambda_R/4$ integration bound is displayed in all three panels with the same dashed black curve. Our site-based Newtonian noise prediction is indicated with a green curve. Left: For a test mass on the surface and a hemispherical cavern with fixed $10\,\text{m}$ radius, our site-based Newtonian noise is lower than the expectation based on Saulson's model due to the incorporation of amplitude attenuation in the seismic field model. Center: For a test mass $1.6\,\text{m}$ above ground our site-based Newtonian noise surpasses analytical surface expectations, as the wave field in close vicinity to the test mass is not neglected since in our calculation no spherical cutoff is applied. Right: For a test mass cavern $50\,\text{m}$ below ground the dominant Rayleigh waves at low frequencies lead to a relatively high site-based Newtonian noise. At frequencies above about $5\,\text{Hz}$ the Rayleigh waves have attenuated and therefore the site-based Newtonian noise decreases, and is derived from low amplitude body waves.*

For this comparison the test mass is located at three distinct locations. First, the test mass is located on the surface with $h = 0$ m, where a hemispherical cavern of constant radius of $10\,\text{m}$ is created around the test mass. A larger fraction of the seismic field in the vicinity of the test mass is included in the volume integral of the site-based Newtonian noise for a fixed cavern radius in comparison to the virtual "cavern" that was created by the frequency dependent cutoff condition. However, the fast attenuation of seismic amplitudes with depth and distance ensures that the site-based Newtonian noise remains below the analytical expectation (Fig. 3.15, left panel). At high frequencies, where Rayleigh wavelengths become smaller than the cavern radius, our site-based Newtonian noise is more strongly suppressed than at low frequencies with respect to the Newtonian noise based on Saulson's analytical expectation.

Second, the test mass is placed at a height of 1.6 m above the ground, which is the same height as the test masses at Advanced Virgo. The test mass height serves as a natural lower cutoff radius for the numerical integral and no additional cutoff from a spherical cavern has been considered. The resulting site-based Newtonian noise therefore does not neglect any seismic displacement in the vicinity of the test mass and the result surpasses the surface Newtonian noise estimates (Fig. 3.15, central panel). The exact noise level depends on the test mass height and decreases with increasing distance from the surface.

The third location of the test mass is at a depth of 50 m, where a fixed cavern radius of 10 m serves as lower integration bound. At this depth the test mass is fully emerged in Rayleigh waves up to a frequency of about 5 Hz and as a result our corresponding site-based Newtonian noise almost reaches the analytical Newtonian noise expectations (Fig. 3.15, right panel). At higher frequencies the Rayleigh waves have attenuated at the depth of the test mass and the wave field consists of body waves. Therefore, our resulting site-based Newtonian noise decreases fast with increasing frequency. For a stronger overall attenuation of Newtonian noise the underground test mass has to be moved to greater depths, be located in a geology with short surface wavelengths or be located in a layered geology where a large fraction of the seismic amplitudes are confined to the surface.

Not only the seismic field and depth of the test mass, but also the cavern shape has influence on our site-based Newtonian noise estimate for an underground detector. For a qualitative study, that neglects scattering of seismic waves on cavity walls, the cavern radius of the test mass at 50 m depth has been successively increased from 5 m to 45 m (see Fig. 3.16). Even though the increasing cavern size suppresses Rayleigh wave amplitudes that would be within the cavern volume below 5 Hz, the higher amplitudes interacting with the larger cavern surface lead to a site-based Newtonian noise that increases with increasing cavern radius. A maximum is reached at 3 Hz, where the cavern diameter is equal to the Rayleigh wavelength. Here, the motion of the cavity wall is coherent in the same direction, which leads to a peak in Newtonian noise. At high frequencies, the waves in close vicinity to the test mass are low-amplitude body waves. Their slowly changing amplitudes cannot compensate for the increasing suppression of nearby seismic displacements as the cavern radius increases and as a result leads to a stronger suppression of our site-specific Newtonian noise at high frequencies. Similar to the maximum at 3 Hz, an increase in Newtonian noise is observed around 18 Hz. Here, the cavern radius is of the order of the P-wavelength, the largest underground wavelength. It is clear that all of these factors depend on
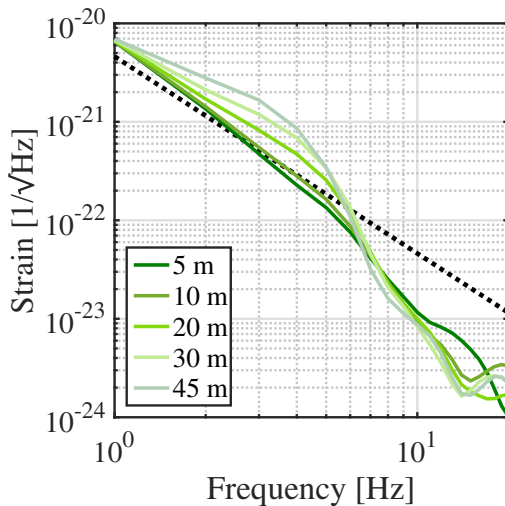

Figure 3.16: *Site-based Newtonian noise for a test mass at 50 m depth for a cavern radius that increases from 5 to 45 m. As the cavern radius increases, Newtonian noise below 5 Hz increases as well, while Newtonian noise at high frequencies decreases. The expectation derived from Saulson's analytical model is depicted with a dashed black curve.*

the local geology, source distribution, seismic field, test mass location and cavern shape and for more insight it will be necessary to study specific examples.

Limitations and possible improvements of the site-based model

Further improvements in the modeling approach of the site-based model are possible. First, a detailed seismic study of the detector site should be conducted to obtain knowledge of the three-dimensional subsurface structure, the mechanism and location of the main seismic sources, as well as PSD and correlation measurements on the surface and underground during longterm periods of at least one year. The geology in the site-based model can be improved by evolving the horizontally layered structure towards a more complex, three-dimensional subsurface composition that encompasses for example fault lines and inclining layers. This migration will require the use of alternative numerical solving software, for instance SOFI3D [131]. Furthermore, the current model derives seismic displacement only from vertical excitations. Including horizontal excitations will improve the agreement between measurement and model at low frequencies, especially if the seismic sources are near the test masses. Far away underground sources will allow to model the so called body wave background, which is not negligible at high frequencies at subsurface detectors sites. In addition, studies for subsurface detectors should move beyond spherical caverns and are advised to investigate the effect of arbitrary cavern shapes and sizes on the Newtonian noise level. It should be noted that in this work the cavern is considered by subtracting the Newtonian noise that is derived within a hypothetical cavern area from the Newtonian noise that is derived if no cavern would be present. Future studies are advised to dedicate time to the investigation of cavern wall motion and its effect on Newtonian noise. As this motion occurs on an interface between soil and air it is potentially non-negligible and its influence is yet to be understood. These factors will improve the agreement between measurement and model output and will lead to an enhanced understanding of site-based Newtonian noise.

Summary

The comparisons shown in this section demonstrate that it is necessary for improved, site-based Newtonian noise estimates at surface and underground detectors to move past a model that is based on Saulson's analytical approach model of Eq. (3.5.2). Our site-based Newtonian noise model is derived from a seismic field that comprises body and surface waves. This seismic field depends on the detector specific geology such as subsurface material composition and the local source distribution. Carrying out a numerical Newtonian noise integration that includes contributions from within the integration volume, from interfaces between subsurface layers and from the boundaries between soil and air is crucial for precise modeling. Furthermore, the test mass location needs to be taken into consideration as well as the cavern geometry. All these parameters depend on a specific detector site and therefore this approach can be used to derive site-based Newtonian noise at various locations of gravitational wave detectors. For our site-based Newtonian noise estimate for Advanced Virgo the reader is referred to Chapter 5 and for our site-based Newtonian noise estimate for an underground detector at the Belgian-German-Dutch Einstein Telescope candidate site in Limburg the reader is referred to Chapter 6.